

# Gravitational Wave Signals from Two-Dimensional Core-Collapse Supernova Models with Rotation and Magnetic Fields

Rylan Jardine<sup>1</sup>, Jade Powell<sup>2</sup>, and Bernhard Müller<sup>1\*</sup>

<sup>1</sup>*School of Physics and Astronomy, Monash University, Clayton, VIC 3800 Australia*

<sup>2</sup>*OzGrav, Centre for Astrophysics and Supercomputing, Swinburne University of Technology, Hawthorn, VIC 3122, Australia*

23 December 2021

## ABSTRACT

We investigate the impact of rotation and magnetic fields on the dynamics and gravitational wave emission in 2D core-collapse supernova simulations with neutrino transport. We simulate 17 different models of  $15 M_{\odot}$  and  $39 M_{\odot}$  progenitor stars with various initial rotation profiles and initial magnetic fields strengths up to  $10^{12}$  G, assuming a dipolar field geometry in the progenitor. Strong magnetic fields generally prove conducive to shock revival, though this trend is not without exceptions. The impact of rotation on the post-bounce dynamics is more variegated, in line with previous studies. A significant impact on the time-frequency structure of the gravitational wave signal is found only for rapid rotation or strong initial fields. For rapid rotation, the angular momentum gradient at the proto-neutron star surface can appreciably affect the frequency of the dominant mode, so that known analytic relations for the high-frequency emission band no longer hold. In case of two magnetorotational explosion models, the deviation from these analytic relations is even more pronounced. One of the magnetorotational explosions has been evolved to more than half a second after the onset of the explosion and shows a subsidence of high-frequency emission at late times. Its most conspicuous gravitational wave signature is a high-amplitude tail signal. We also estimate the maximum detection distances for our waveforms. The magnetorotational models do not stick out for higher detectability during the post-bounce and explosion phase.

**Key words:** transients: supernovae – gravitational waves – magnetic fields – MHD

## 1 INTRODUCTION

After the groundbreaking detection of gravitational waves (GWs) from merging compact binaries (Abbott et al. 2016, 2017), the new field of GW astronomy still faces further challenges. Among the yet undetected sources of GWs, explosions of massive stars as core-collapse supernovae (CCSNe) are a coveted target. The detection of a CCSN in our own galaxy or its satellites could shed significant insights on the inner workings of the explosions, the rotational state of the progenitor stars, the structure of the newly born compact remnant, and the nuclear equation of state (for a review, see Kotake & Kuroda 2017; Kalogera et al. 2019; Abdikamalov et al. 2020).

In order to optimise the chances of a detection and maximise the scientific insights from a prospective nearby event, it is critical to thoroughly investigate the structure and physical dependencies of the CCSN GW signal from the collapse to the post-explosion phase based on a broad exploration of factors that influence the dynamics in the supernova core, such as progenitor mass, rotation, magnetic fields, and the nuclear equation of state. The first phase of GW emission in CCSNe, the signal from the collapse and bounce of rotating iron cores is already well understood (Dimmelmeier et al. 2008; Abdikamalov et al. 2014; Richers et al. 2017) to the point that it could be used to quantitatively constrain the rotation of the progenitor core in the case of a Galactic event. The impact of mag-

netic fields on the bounce signal has also been investigated (Obergaullinger et al. 2006; Scheidegger et al. 2008). Although less apparent at first glance, the GW signal from the post-bounce phase has also been shown to contain clear fingerprints of the structure of the newly born proto-neutron star (PNS) and the dynamics in the supernova core (e.g., Müller et al. 2013; Cerdá-Durán et al. 2013; Sotani & Takiwaki 2016; Morozova et al. 2018; O’Connor & Couch 2018; Torres-Forné et al. 2018; Andresen et al. 2019; Powell & Müller 2019; Radice et al. 2019; Pan et al. 2021; Mezzacappa et al. 2020). The time-frequency structure of the post-bounce signal shows distinct emission bands that reveal the frequencies of quadrupolar PNS oscillation modes – the most prominent one being an  $l = 2$  g- mode, later often replaced by the fundamental f- mode frequency after several hundred milliseconds (Morozova et al. 2018; Torres-Forné et al. 2018; Sotani & Takiwaki 2020) – and in some models (Kuroda et al. 2016; Andresen et al. 2017; Powell & Müller 2020) the standing accretion shock instability (SASI; Blondin et al. 2003; Blondin & Mezzacappa 2006; Foglizzo et al. 2007), and possibly a triaxial corotation instability in the case of extremely rapid rotation (Kuroda et al. 2014). In recent years, it has become possible to rigorously identify the nature of underlying oscillation modes in the spectrograms by means of a linear eigenmode analysis. While the frequency of the characteristic emission bands reveal the *structure* of the PNS and its environment, the amplitudes of the various signal components reflect dynamics in the supernova core, i.e., the violence of oscillatory

\* bernhard.mueller@monash.edu

instabilities and of the turbulent flow that excites PNS oscillations (Radice et al. 2019; Powell & Müller 2019).

For CCSNe of non-rotating progenitors, the f/g-mode emission band and the SASI emission band can be described by simple, “universal” scaling laws in terms of the PNS mass, radius, and surface temperature, and the shock radius (Torres-Forné et al. 2019). In the case of a GW detection with a sufficiently high signal-to-noise ratio, these relations could potentially be exploited to quantitatively constrain PNS and shock parameters. For non-rotating models, the overall signal strength (as quantified by the peak amplitude and overall energy emitted in GWs) also shows correlations with the progenitor core mass and a trend towards stronger GW emission in the case of successful explosions (Müller et al. 2013; Radice et al. 2019; Powell & Müller 2019). This may provide further qualitative clues about the progenitor and the explosion dynamics in the case of a Galactic supernovae. These patterns emerge fairly consistently among the manifold 2D (Müller et al. 2004; Marek et al. 2009; Yakunin et al. 2010; Müller et al. 2013; Yakunin et al. 2015; Morozova et al. 2018; Pajkos et al. 2019) and 3D (Kuroda et al. 2016; Andresen et al. 2017; Powell & Müller 2019; Radice et al. 2019; Mezzacappa et al. 2020; Powell & Müller 2020; Powell et al. 2021) studies of the GW signal based on modern neutrino radiation hydrodynamics simulations of non-rotating progenitors despite differences in detail in mode frequencies and GW amplitudes.

However, this picture of GW emission from the post-bounce phase may be substantially affected by rotation and magnetic fields. Already on their own rapid rotation (Kuroda et al. 2014; Takiwaki & Kotake 2018; Summa et al. 2018) and strong magnetic fields (Obergaullinger et al. 2014; Müller & Varma 2020; Matsumoto et al. 2020) can each have a significant impact on CCSN dynamics. Acting in tandem, rapid rotation and strong magnetic fields can give rise to powerful magnetorotational explosions, which have already been explored very actively by means of 2D and 3D simulations (Burrows et al. 2007; Winteler et al. 2012; Mösta et al. 2014; Obergaullinger & Aloy 2017; Mösta et al. 2018; Obergaullinger & Aloy 2020; Kuroda et al. 2020; Obergaullinger & Aloy 2021). The major impact of rapid rotation and/or magnetic fields is bound to leave an imprint on the GW signal as well. Several studies have already shown that (in addition to producing the characteristic bounce signal) rotation can substantially alter the mode frequencies, affect the amplitudes of different components of the GW signal, and give rise to new, powerful signal features (Andresen et al. 2019; Powell & Müller 2020; Pajkos et al. 2019; Kuroda et al. 2014; Shibagaki et al. 2020). The combined impact of rotation and magnetic fields on the GW signal still merits further investigation, however. Studies of GW emission from rotating magnetised stellar cores have so far been confined to the collapse, bounce, and early post-bounce phase (Obergaullinger et al. 2006; Scheidegger et al. 2010; Takiwaki & Kotake 2011). Waveform predictions from anelastic long-time magnetohydrodynamic (MHD) simulations of PNS convection in rapidly rotating neutron stars have recently also become available (Raynaud et al. 2022). The impact of magnetic fields in non-rotating models (Obergaullinger et al. 2014) and the combined impact of rotation and magnetic fields (Obergaullinger & Aloy 2020) on supernova dynamics have been explored more systematically across a wider range of the parameter space already by means of long-time simulations including MHD and neutrino transport, but for the GW signal, such an exploration of parameter space is still lacking.

In this paper, we therefore conduct a suite of 17 axisymmetric (2D) MHD simulations with the CoCoNuT-FMT code to produce gravitational waveforms over a range of initial magnetic fields and rotation rates for two different CCSN progenitors, a 15  $M_{\odot}$  red su-

pergiant (Heger et al. 2005) and a 39  $M_{\odot}$  helium star (Aguilera-Dena et al. 2018). We analyse the combined effect of rotation and magnetic fields on the overall strength of the GW emission and the characteristic features in the GW spectrogram, and estimate detection distances for our models. We also investigate the impact of rotation and magnetic fields on the pre-explosion and explosion dynamics to complement and corroborate the aforementioned parameter studies of Obergaullinger et al. (2014); Matsumoto et al. (2020).

Our paper is structured as follows. In Section 2 we describe the numerical methods and microphysics used in our simulations. The progenitor models and our choice of initial conditions for the pre-collapse rotation profiles and magnetic fields are discussed in Section 3. In Section 4, we first review the dynamical evolution of our models, and then analyse their GW emission. We summarise our findings, discuss their implications, and outline questions for future work in Section 5.

## 2 NUMERICAL METHODS

We analyse the GW emission in several 2D simulations performed with the Newtonian version of the neutrino MHD code CoCoNuT-FMT. The equations of Newtonian MHD are solved in spherical polar coordinates using a finite-volume scheme employing higher-order reconstruction and the HLLC solver of Gurski (2004); Miyoshi & Kusano (2005), in conjunction with hyperbolic divergence cleaning (Dedner et al. 2002). The MHD equations for the density  $\rho$ , magnetic field  $\mathbf{B}$ , total energy density  $e$ , velocity  $\mathbf{v}$  and Lagrangian multiplier  $\psi$  are expressed in Equations (1)–(5) in Gaussian units including divergence cleaning terms as

$$\partial_t \rho + \nabla \cdot (\rho \mathbf{v}) = 0, \quad (1)$$

$$\partial_t (\rho \mathbf{v}) + \nabla \cdot \left[ \rho \mathbf{v} \mathbf{v}^T + \left( p + \frac{\mathbf{B}^2}{8\pi} \right) \mathbf{I} - \frac{\mathbf{B} \mathbf{B}^T}{4\pi} \right] = \rho \mathbf{g} + \mathbf{Q}_m - \frac{(\nabla \cdot \mathbf{B}) \mathbf{B}}{4\pi}, \quad (2)$$

$$\partial_t \mathbf{B} + \nabla \cdot (\mathbf{v} \mathbf{B}^T - \mathbf{B} \mathbf{v}^T + \psi \mathbf{I}) = 0, \quad (3)$$

$$\partial_t e + \nabla \cdot \left[ \left( e + p + \frac{\mathbf{B}^2}{8\pi} \right) \mathbf{v} - \mathbf{B} (\mathbf{v} \cdot \mathbf{B}) \right] = \rho \mathbf{v} \cdot \mathbf{g} + Q_e + \mathbf{Q}_m \cdot \mathbf{v} - \frac{\mathbf{B} \cdot \nabla (c_h \psi)}{4\pi}, \quad (4)$$

$$\partial_t \psi + c_h \nabla \cdot \mathbf{B} = -\frac{\psi}{\tau}. \quad (5)$$

Here  $c_h$  denotes the hyperbolic cleaning speed,  $p$  the gas pressure,  $\tau$  the damping time for the Lagrangian multiplier, and  $Q_e$  and  $\mathbf{Q}_m$  are the neutrino energy and momentum source terms. The cleaning speed  $c_h$  is identified with the fast magnetosonic velocity, and the damping time is set to eight times the magnetosonic crossing time of a cell. Note that we use a symmetrised form of the cleaning terms, which gives  $\psi$  the same dimension as the magnetic field and has superior stability properties. One of our models (m15afB12, Section 3) was recalculated with the cleaning scheme of Müller & Varma (2020) to improve stability during the explosion phase and eliminate occasional rapid oscillations in the time step limit. We utilise the effective relativistic potential of case ‘Arot’ in Müller et al. (2008).

The fast multi-group transport (FMT) method of Müller & Janka (2015) is used for the neutrino transport, to obtain the neutrino source terms  $\mathbf{Q}_m$ ,  $Q_e$ , and  $Q_{Y_e}$  in the momentum and energy equations (2,4), and the electron number source term in the equation for the electron fraction  $Y_e$ ,

$$\partial_t (\rho Y_e) + \nabla \cdot (\rho \mathbf{v} Y_e) = Q_{Y_e}. \quad (6)$$

We use a spatial resolution of  $550 \times 128$  in radius  $r$  (with non-equidistant spacing) and angle  $\theta$ , and energy groups for our neutrino transport. At high densities, we employ the equation of state of Lattimer & Swesty (1991) with a bulk incompressibility of  $K = 220$  MeV. The low-density equation of state accounts for an ideal gas of nuclei alongside photons, electrons and positrons combined with a flashing treatment for nuclear reactions (Rampp & Janka 2002).

The innermost 10 km of the grid are treated using a spherical 1D grid. In the 1D core region, all thermodynamic quantities and the meridional velocity component are assumed to be spherically symmetric. However, the 1D core is allowed to rotate rigidly, and contains a divergence-free magnetic field with a constant component  $B_z$  along the grid axis, and a constant toroidal field  $B_\phi$ .

### 3 PROGENITOR MODELS AND SIMULATION SETUP

We simulate 17 different models using two different progenitor stars, namely the  $15 M_\odot$  progenitor m15b6 from Heger et al. (2005) and the  $39 M_\odot$  progenitor m39 from Aguilera-Dena et al. (2018). The parameters of the 17 models are summarised in Table 1. The model labels denote the progenitor (m15 or m39), the initial rotation profile, and the initial magnetic field strength, e.g., model m15nrB10 uses the  $15 M_\odot$  progenitor with no rotation and an initial maximum field strength of  $10^{10}$  G. The progenitor models, rotation profiles, and initial magnetic field configurations are explained in more detail below.

Model m15b6, has been evolved up to collapse using the stellar evolution code KEPLER with magnetic torques (Heger et al. 2005) based on the Tayler-Spruit dynamo (Spruit 1999, 2002), and has a moderate core spin rate. Its central rotation rate, of  $0.05 \text{ rad s}^{-1}$  at the onset of collapse translates to a birth spin period of  $\sim 11$  ms for a nascent neutron star assuming that angular momentum is not exchanged between the collapsing core and the ejecta during the explosion. This amounts to a rotational energy of  $\sim 2 \times 10^{50}$  erg, too low to power a CCSN by magnetorotational effects alone. The default progenitor rotation profile of m15b6 is denoted ‘ps’ (in the model labels) for ‘progenitor, slow rotation’ in Table 1.

We also simulate model m15b6 without rotation (model label ‘nr’ for no rotation) and with a artificial fast rotation profile, labelled ‘af’ in the model names. The ‘af’ profile is adapted from the ‘artrot’ profile used previously in the works Summa et al. (2018); Müller et al. (2004); Buras et al. (2006); Marek & Janka (2009) and involves a rotation profile that changes from uniform to differential rotation at the edge of the iron core. For model m15b6, it entails a constant angular velocity of  $\Omega = 0.5 \text{ rad s}^{-1}$  within the iron core,  $r < 1500$  km. Outside of the core the angular velocity decreases as  $\Omega \propto r^{-3/2}$ .

Model m39 (Aguilera-Dena et al. 2018) is a rapidly rotating Wolf-Rayet star with a low metallicity of  $1/50 Z_\odot$ , a pre-collapse mass of  $22 M_\odot$  and an initial helium star mass of  $39 M_\odot$ . The model has been computed using MESA (Modules for Experiments in Stellar Astrophysics; Paxton et al. 2013), again using magnetic torques following Spruit (2002) and Heger et al. (2005). Starting with a fast initial surface rotation velocity of  $600 \text{ km s}^{-1}$ , the model retains substantial angular momentum in the core such that it would collapse to a neutron star with a spin period of  $\sim 4.15$  ms under the assumption of angular momentum conservation, and with a rotational energy of  $2.6 \times 10^{51}$  erg, sufficient to undergo a magnetorotational explosion with moderate energy. The high initial mass of the star is thought to be sufficient for the model to form a black hole with a mass of  $\sim 5 M_\odot$ . Additionally, the high specific angular momentum  $j$  in the

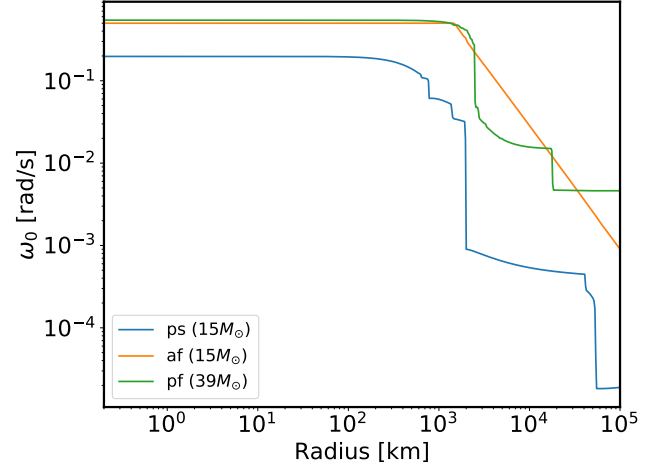


**Figure 1.** Initial rotation profiles of each of our models at the onset of collapse.

shells surrounding the core ( $j = 9.36 \times 10^{15} \text{ cm}^2 \text{ s}^{-1}$  at  $5 M_\odot$ ) implies the progenitor would also be a candidate for a hypernova explosion and long duration gamma-ray burst (IGRB) within the collapsar model. This model was investigated both with its default rotation profile from the stellar evolution calculation (model label ‘pf’ for ‘progenitor, fast rotation’) and also without rotation (model label ‘nr’). The initial core angular velocities,  $\omega_0$ , are presented in Table 1 and initial rotation profiles are presented in Figure 1.

For both progenitors and every rotation profile, we investigate models with initial maximum field strengths  $b_{p,0}$  and  $b_{t,0}$  for the poloidal and toroidal component of the magnetic field of 0 G,  $10^{10}$  G and  $10^{12}$  G in the stellar core. In addition, one model, m15psB11, with a field strength of  $10^{11}$  G was included for the  $15 M_\odot$  progenitor with the default rotation profile. In all cases the initial magnitudes of both the toroidal and poloidal components of the magnetic field were identical.

We employ a dipole magnetic field geometry similar to the implementation of Obergaulinger & Aloy (2017), taking the following form:

$$(A_r, A_\theta, A_\phi) = \left( r b_{t,0} \frac{r_0^3}{(r_0^3 + r^3)} \cos \theta, 0, \frac{r}{2} b_{p,0} \frac{r_0^3}{(r_0^3 + r^3)} \sin \theta \right), \quad (7)$$

with  $r_0 = 10^8$  cm.

The actual magnetic field strengths in the core and inner shells of massive stars are somewhat uncertain. A range of plausible estimates can be made based on white dwarf magnetic fields (Ferrario & Wickramasinghe 2006; Ferrario et al. 2015), dynamo models for radiative zones (Heger et al. 2005), and equipartition arguments for the field in convective zones (Christensen et al. 2009; Müller & Varma 2020). The field geometry is even more uncertain. Following previous studies of MHD effects in non-rotating (Obergaulinger et al. 2014; Matsumoto et al. 2020) and rotating (e.g., Burrows et al. 2007; Suwa et al. 2007; Winteler et al. 2012; Mösta et al. 2014; Obergaulinger & Aloy 2017, 2020; Kuroda et al. 2020) CCSN models, we use initial fields of  $10^{10}$  G and  $10^{12}$  G, to study the impact of moderate and high magnetisation on the dynamics and the GW signal, respectively, and contrast these with non-magnetised models as controls. Pre-collapse fields of  $10^{12}$  G are sufficiently high to reach dynamically relevant field strengths (for powering magnetically-dominated explosions) via field compression during collapse alone, whilst secondary amplification mechanisms like the magnetorotational insta-

bility (Balbus & Hawley 1991; Akiyama et al. 2003) or an  $\alpha$ - $\Omega$  dynamo (Thompson & Duncan 1993; Raynaud et al. 2020) would be required to reach this regime from an initial field strength of  $10^{10}$  G. Random density fluctuations of  $10^{-4}$  were applied in all cells at the onset of collapse in the non-rotating and non-magnetic models m15nrB0 and m39nrB0 in order to break spherical symmetry. No explicit perturbations were added in the other models.

## 4 RESULTS

### 4.1 Impact of Rotation and Magnetic Fields on Post-Bounce Dynamics

A summary of the simulation outcomes for all models, and if applicable, the explosion times and energies can be found in Table 1 which illustrates the sensitivities of the dynamical evolution to the initial rotation rate and field strength. The explosion energies given in the table are “diagnostic energies” at the end of the simulations (Buras et al. 2006), i.e., they are computed as the integral of the net total (kinetic, internal, magnetic, and potential) energy over the material that is nominally unbound. Angle-averaged shock radii for all models are presented in Figure 2. Our models substantially conform to the trends and effects seen in previous systematic studies of rotation in non-magnetised supernova simulations (Summa et al. 2018), and magnetic fields in non-rotating models (Obergaullinger et al. 2014; Matsumoto et al. 2020). We therefore confine ourselves to a brief descriptive discussion of the post-bounce dynamics of our models, which mainly serves to set the ground for the subsequent analysis of the GW signals.

We find a general trend towards earlier shock revival with rotation and with higher initial magnetic field strength. Trends in explosion energy  $E_{\text{expl}}$  are more difficult to discern because  $E_{\text{expl}}$  generally has not asymptoted to its final values at the end of the simulations yet. However, the hierarchy of the explosion energies at the end of the simulations in Table 1 generally reflects the hierarchy during the entire rise phase and is not just a momentary snapshot. The rapidly rotating and strongly magnetised model m15afB12 is the only one to exceed  $10^{51}$  erg, even though it is still not in the hypernova regime with  $E_{\text{expl}} = 1.4 \times 10^{51}$  erg at the end of the simulation. There are, however, significant exceptions to this trend that are in line with effects observed in the literature and are best illustrated by discussing the  $15 M_{\odot}$  and  $39 M_{\odot}$  progenitors separately.

#### 4.1.1 $15 M_{\odot}$ models

For the  $15 M_{\odot}$  models, we invariably find that higher magnetisation leads to an earlier explosion, irrespective of the progenitor’s rotation profile. This is consistent with the findings of Obergaullinger et al. (2014) for non-rotating progenitors. Specifically, the  $10^{12}$  G case is the only one among the non-rotating model to develop an explosion because the initial field is strong enough to roughly reach equipartition between magnetic and kinetic energy in the gain region after collapse so that the fields substantially shape the post-shock flow, similar to the strong-field ( $10^{12}$  G) model of Obergaullinger et al. (2014).

Interestingly, for the default rotation profile, even a “weak” initial magnetic field of  $10^{10}$  G makes a difference between explosion and failure (Figure 2a). However, this does not necessarily indicate a robust effect of such weak fields on shock revival. A comparison with the literature shows that the  $15 M_{\odot}$  model is on the margin between explosion and failure. For example, regardless of rotation rate, none

of our  $15 M_{\odot}$  models explode *without* including magnetic fields, nor do the models of Pajkos et al. (2019) for the same progenitor (even though they did not evolve their simulations far beyond 300 ms post-bounce). By contrast, the 2D models with no rotation and default rotation in Summa et al. (2018) develop an explosion (whereas their 3D counterparts do not). Under such circumstances, even a minor impact of the (dipole) magnetic field on the growth of instabilities in the post-shock region in the m15ps models can tilt the balance towards shock revival by slightly facilitating the emergence of an  $\ell = 1$  mode in the flow (Figure 3) so that the shock is already more extended when the Si/O shell interface reaches the shock around 0.2 s after bounce (Figure 2a). It must be borne in mind that such subtle effects may generally be swamped by stochastic model variations even though they can be diagnosed for precisely controlled seed perturbation for non-radial instabilities as in our magnetic models.

While magnetic fields always prove beneficial for shock revival in the m15 series, the effect of rotation is non-monotonic, i.e., a higher rotation rate in 2D does not guarantee a greater likelihood of explosion, which is consistent with Summa et al. (2018). The m15nr and m15af models do not explode except in the presence of strong initial fields of  $10^{12}$  G. As pointed out in the literature, such non-monotonicities arise due to competing effects in rotating models. On the one hand greater centrifugal support provided by rotation is expected to lead to an extended shock front and, in turn, larger gain region and thus stronger neutrino heating (Summa et al. 2018), which can also be seen in the comparison of the late-time shock trajectory of model m15afB0 vis á vis m15psB0 and m15nrB0. The resulting increase of the mass in the gain region can be compensated by lower neutrino luminosities and mean energies (Summa et al. 2018) due to the larger radius of a PNS with substantial centrifugal support. Furthermore, as pointed out by (Pajkos et al. 2019), rotation can also hurt shock revival because a positive angular momentum inherited from the progenitor can inhibit convection in the gain region according to the Solberg–Høiland criterion (e.g., Kippenhahn et al. 2012; Maeder et al. 2013).<sup>1</sup> The analytic rotation profile chosen for the m15af series indeed exhibits a positive angular momentum gradient. The specific angular momentum  $j_z$  scales as  $j_z \propto r^2$  inside the core and  $j_z \propto r^{1/2}$  outside the core, and hence the angular momentum gradient may contribute to the lower explodability of the m15af series compared to the m15ps models. We stress, however, that the impact of rotation can be qualitatively different in 3D, where the beneficial effects of a strong spiral mode of the SASI (Summa et al. 2018), or the low- $|T|/W$  instability (Takiwaki et al. 2016) for rapidly spinning progenitors outweigh the adverse effects of rotation. As expected, adverse effects of rotation are also overcome in 2D in the presence of strong magnetic fields. Model m15afB12 develops a classical early bipolar explosion as familiar from 2D simulations of magnetorotational explosions (Burrows et al. 2007; Sawai et al. 2008; Obergaullinger & Aloy 2017, 2020) with a rapid growth of the explosion that has reached  $8.6 \times 10^{51}$  erg and is still increasing at this point.

#### 4.1.2 $39 M_{\odot}$ models

The  $39 M_{\odot}$  models present an even more intricate picture. Different from the m15 series, all the rotating  $39 M_{\odot}$  models develop explosions. Rotation precipitates shock revival in the non-magnetised

<sup>1</sup> As noted by Andresen et al. (2019), rotation can also inhibit convection in the proto-neutron star convection zone, which has implications for gravitational wave emission.



Name	$M$ ( $M_{\odot}$ )	$B$ (G)	Rotation profile	$\omega_0$ ( $\text{rad s}^{-1}$ )	$t_{\text{exp}}$ (s)	$E_{\text{expl}}$ ( $10^{50}$ erg)	Explosion mechanism	$E_{\text{GW}}$ ( $10^{46}$ erg)	$f_p$ (Hz)	$A_{20,\text{max}}^{\text{E2}}$ (cm)
m15psB0	15	0	progenitor, slow	$2.0 \times 10^{-1}$	DNE	—	—	$> 2.28$	700	47
m15psB10	15	$10^{10}$	progenitor, slow	$2.0 \times 10^{-1}$	0.28	0.34	neutrino-driven	$> 5.20$	1240	58
m15psB11	15	$10^{11}$	progenitor, slow	$2.0 \times 10^{-1}$	0.23	0.49	neutrino-driven	$> 4.87$	950	46
m15psB12	15	$10^{12}$	progenitor, slow	$2.0 \times 10^{-1}$	0.20	$> 4.54$	neutrino-driven	$> 6.25$	700	76
m15afB0	15	0	artificial, fast rotation	$5.0 \times 10^{-1}$	DNE	—	—	$> 1.29$	1350	50
m15afB10	15	$10^{10}$	artificial, fast	$5.0 \times 10^{-1}$	DNE	—	—	$> 0.98$	730	40
m15afB12	15	$10^{12}$	artificial, fast	$5.0 \times 10^{-1}$	0.16	$> 86.48$	magnetorotational	$> 1.24$	450	56
m15nrB0	15	0	no rotation	0	DNE	—	—	$> 3.78$	1160	33
m15nrB10	15	$10^{10}$	no rotation	0	DNE	—	—	$> 1.99$	1230	38
m15nrB11	15	$10^{11}$	no rotation	0	DNE	—	—	$> 1.79$	1650	42
m15nrB12	15	$10^{12}$	no rotation	0	0.44	$> 1.01$	neutrino-driven	$> 2.49$	1370	67
m39pfB0	39	0	progenitor, fast	$5.4 \times 10^{-1}$	0.33	$> 2.36$	neutrino-driven	$> 39.07$	1140	99
m39pfB10	39	$10^{10}$	progenitor, fast	$5.4 \times 10^{-1}$	0.40	$> 3.70$	neutrino-driven	$> 45.23$	1460	76
m39pfB12	39	$10^{12}$	progenitor, fast	$5.4 \times 10^{-1}$	0.16	$> 6.25$	magnetorotational	$> 9.03$	990	62
m39nrB0	39	0	no rotation	0	DNE	—	—	$> 23.55$	1440	98
m39nrB10	39	$10^{10}$	no rotation	0	0.26	$> 5.67$	neutrino-driven	$> 27.35$	1310	108
m39nrB12	39	$10^{12}$	no rotation	0	$\sim 0.5^{\dagger}$	$> 0.25$	neutrino-driven	$> 11.36$	1790	57

**Table 1.** Initial conditions and key outcomes for the CCSN simulations performed in this study.  $M$  is the progenitor mass; simulations with  $15 M_{\odot}$  use progenitor model m15b6, whilst  $39 M_{\odot}$  models use m39.  $B$  denotes the initial toroidal and poloidal magnetic field strengths at the centre of the star. The rotation profiles are described in detail in Section 3.  $\omega_0$  is the central angular velocity  $\omega_0$ ; for detailed rotation profiles see Figure 1.  $t_{\text{exp}}$  denotes the time of explosion, defined as the time at which the average shock radius exceeds 500 km, to the nearest 10 ms. Entries ‘DNE’ (‘does not explode’) denote models without shock revival.  $E_{\text{expl}}$  is the diagnostic explosion energy at the end of the simulation, and ‘explosion mechanism’ specifies whether the explosion (if one occurs) is neutrino-driven or magnetorotational.  $E_{\text{GW}}$  gives the energy emitted in GWs,  $f_p$  the frequency corresponding to the peak of the GW energy spectrum, and  $A_{20,\text{max}}^{\text{E2}}$  is the peak amplitude of GWs prior to the tail phase.

<sup>†</sup> As seen in Figure 2e, while the shock has not yet reached a radius of 500 km within the time of the simulation, model m39nrB12 is clearly in the process of exploding.

models and the  $10^{12}$  G models, but delays shock revival slightly for an initial field of  $10^{10}$  G. It is noteworthy that the  $39 M_{\odot}$  progenitor exhibits a negative gradient in specific angular momentum at the Si/O shell interface (Powell & Müller 2020), which may explain why rapid progenitor rotation is not hurtful in the non-magnetised case, different from the  $15 M_{\odot}$  model. However, in contrast to the  $15 M_{\odot}$  models, we also find non-monotonic behaviour with respect to the initial field strength. For the unmodified progenitor rotation profile (which is tantamount to rapid rotation in this case), the weak-field model m39pfB10 explodes considerably later than the non-magnetised and strongly magnetised models (Figure 2d). The non-rotating series m39nr is even more interesting (Figure 2e). Here the weak-field model m39nrB10 explodes early about 0.26 s after bounce, m39nrB0 does not explode at all, and the strong-field model m39nrB12 explodes with a considerable delay around half a second after bounce. The significant delay of shock revival in model m39nrB12 compared to m39nrB10 is unexpected and to be contrasted with the findings of Obergaulinger et al. (2014), where strong initial fields help bring about an earlier explosion. Close inspection reveals that model m39nrB12 just narrowly misses an explosion at the same time as m39nrB10; the critical ratio between the advection time scale  $\tau_{\text{adv}}$  and the heating time scale  $\tau_{\text{heat}}$  (Buras et al. 2006)

comes close to unity before turning around and only reaching the explosion threshold about 250 ms later (Figure 4, bottom). This can be explained by slightly smaller turbulent kinetic energy  $E_{\text{turb}}$  in the gain region, which can be computed as

$$E_{\text{turb}} = \frac{1}{2} \int \rho [(v_r - \langle v_r \rangle)^2 + v_{\theta}^2] dV, \quad (8)$$

where  $v_r$  and  $v_{\theta}$  are the velocity components in the radial and meridional direction, and  $\langle v_r \rangle$  is the mass-weighted spherical average of the radial velocity (Figure 4, top). The adverse effects of strong magnetic fields on the explosion conditions is reminiscent of the convection-dominated  $15 M_{\odot}$  model of Matsumoto et al. (2020), who found that strong initial fields can suppress the growth of medium- to small-scale turbulence, and thereby reduce the overall turbulent kinetic energy stored in the gain region. We note, however, that the situation was reversed for the  $15 M_{\odot}$  model (Section 4.1.1), where a strong seed field of  $10^{12}$  G resulted in an explosion whereas fields of  $10^{10}$  G and  $10^{11}$  G did not. Hence we cannot yet robustly reproduce a suppression effect that is detrimental to shock revival. Different seeds for the growth of neutrino-driven convection (dipole perturbation vs. random perturbations) may account for the divergence between the weak-field runs ( $10^{10}$  G) and the corresponding non-magnetised runs.

Again, the combination of rapid rotation and strong magnetic fields in model m39pfB12 leads to a characteristic bipolar explosion geometry in which magnetic fields clearly shape the flow into collimated outflows. Compared to the  $15 M_{\odot}$ , the one case that develops a true magnetorotational explosion among the  $39 M_{\odot}$  models sticks out less prominently in terms of shock propagation and explosion energetics; the explosion energy has only reached  $6.25 \times 10^{50}$  erg by the end of the simulation. However, the explosion morphology of this model remains very distinct. Compared to model m39pfB10, which develops a neutrino-driven explosion, m39pfB12 exhibits a much more prolate explosion geometry, no volume-filling turbulence in the post-shock region, and early quenching of accretion downflows in the equatorial plane (Figure 5).

## 4.2 Gravitational Wave Signals

The main focus of this paper is investigating the impact of magnetisation and rotation on the GW signal. To this end, we compute the GW amplitude  $A_{20}^{E2}$ , which is the only non-vanishing quadrupole component in the decomposition of the far-field metric perturbations into pure-spin tensor harmonics (Thorne 1980) in axisymmetry.  $A_{20}^{E2}$  can be calculated in spherical polar coordinates in axisymmetry using the time-integrated quadrupole formula (Finn 1989; Blanchet et al. 1990; Kotake et al. 2004),

$$A_{20}^{E2}(t) = \frac{G}{c^4} \frac{16\pi^{3/2}}{\sqrt{15}} \frac{d}{dt} \int_{-1}^1 \int_0^{\infty} \rho(r, z, t) v_r \left( \frac{3}{2} z^2 - 1 \right) - 3v_{\theta} z \sqrt{1 - z^2} dr dz,$$

where  $z = \cos(\theta)$  and  $\rho$  is the rest mass density. The velocity,  $v_i$ , is expressed in terms of unit vectors in the  $r$ ,  $\theta$  and  $\phi$  directions. Note that the magnetic field does not enter in the time-integrated Newtonian quadrupole formula, different from the stress formula (Obergaullinger et al. 2006). For an observer located at an angle  $\theta$  from the symmetry axis of the source, at distance  $R$ , the dimensionless GW strain,  $h$  can be computed from  $A_{20}^{E2}$  as (see, e.g., Mueller & Janka 1997)

$$h = \frac{1}{8} \sqrt{\frac{15}{\pi}} \sin^2 \theta \frac{A_{20}^{E2}(t)}{R}. \quad (9)$$

We do not include the GW signal from anisotropic neutrino emission (Epstein 1978) in this work, which only adds a low-frequency contribution and usually does not significantly increase the detectability of the signal in currently operating detectors.

We show gravitational waveforms for all our models (except m15psB11 and m15nrB11, which do not fit into the  $3 \times 3$ -tableau) in Figures 6 and 7, and spectrograms in Figures 8 and 9. The spectrograms are constructed using a discrete short-time Fourier transform with a Blackman window function (Blackman & Tukey 1958) of width 31.25 ms.

### 4.2.1 Quasi-periodic Early Signal and Quiescent Period

During the first  $\sim 100$  ms after bounce, the characteristics of the GW emission in our models conform to the usual behaviour observed in 2D models (Murphy et al. 2009; Marek et al. 2009; Yakunin et al. 2010, 2015; Müller et al. 2013; Mezzacappa et al. 2020). There is no prominent signal from rotational bounce, even in the m15af and m39 models with relatively fast core rotation, where it is artificially suppressed because we treat the density and velocity field as spherically symmetric in the innermost 10 km of the computational domain. During the first  $\sim 30$ –50 ms, all models show the characteristic quasi-periodic signal with amplitudes of a few 10 cm as typical for 2D

models, which is due to the “ringing” of the shock and acoustic wave propagation in the wake of prompt convection (Yakunin et al. 2010; Müller et al. 2013). The spectrograms show broadband power from 0 to  $\sim 1000$ –2000 Hz, with a peak around 100–200 Hz, although it is difficult to see the high frequency emission due to its transient nature. The quasi-periodic signal is followed by a relatively quiescent period of GW emission until  $\sim 100$  ms after bounce; some models show some recognisable activity at 100–200 Hz due to early SASI activity during this phase. The periods of early SASI oscillations tend to be of order 20 ms (cp. Figure 3), which is consistent with the low-frequency features in the waveforms if frequency doubling is taken into account (Andresen et al. 2017). A precise matching of the gravitational wave frequency with the time-frequency structure of the shock oscillations is difficult because in addition to frequency doubling, (weak) quadrupole modes of the SASI may also contribute to gravitational wave emission (Andresen et al. 2017).

The amplitudes of the quasi-periodic signal differ by a factor of several for different models of a given progenitor. For example, model m39pfB0 sticks out with a peak amplitude of almost 100 cm compared to about 30 cm in m39nrB10 and m39nrB12. However, the amplitudes of the early quasi-periodic signal are known to be affected strongly by stochasticity. We therefore cannot identify any clear trends with rotation and initial magnetic field strengths in our models; all features of the GW signal are well within the confines of non-rotating, non-magnetised 2D models during this phase.

### 4.2.2 GW Signal from Convection and the SASI

Subsequently, the models still largely conform to the typical GW emission patterns known from 2D and 3D models during the pre-explosion and early explosion phase, although important differences to the canonical picture emerge especially in case of the magnetorotational explosion models m15afB12 and m39pfB12 upon closer inspection.

Thus, from  $\sim 100$  ms after bounce neutrino-driven convection and PNS convection start to shape the GW signal by exciting various oscillation modes, specifically a dominant high-frequency emission band from a quadrupolar f/g-mode (Müller et al. 2013; Morozova et al. 2018; Torres-Forné et al. 2018). In some cases, there is strong SASI activity that directly translates into a low-frequency GW emission band. The amplitudes of the models during the pre-explosion phase are quite similar for a given progenitor. Rotation and magnetic field primarily exert an indirect influence on GW emission caused by convection and the SASI by influencing the conditions for explosion; in models that undergo shock revival, GW emission characteristically ramps up for a few 100 ms (Müller et al. 2013), whereas the rapidly rotating models m15afB0 and m15afB10 betray a more direct effect of rotation on GW emission because they have significantly lower GW amplitudes than their counterparts with no or slow rotation. This is in line with the findings of Andresen et al. (2019), who found that high-frequency GW emission is suppressed for strong rotation because of the stabilising influence of positive angular momentum gradients on convection. Different from the 3D model m15fr of Andresen et al. (2019) which showed strong GW emission from the spiral mode of the SASI, there is nothing to compensate for the reduced high-frequency emission, and the overall effect of rapid rotation is a reduction of the GW amplitudes.

Many (but not all) of the differences in the spectrogram can also be explained by the presence or absence of shock revival. For example, for the non-exploding  $15 M_{\odot}$  models in Figure 8 a), d), e), g) and h), we see low-frequency SASI emission in contrast to the exploding models in panels b), c), f), and i), which afterwards dies off.

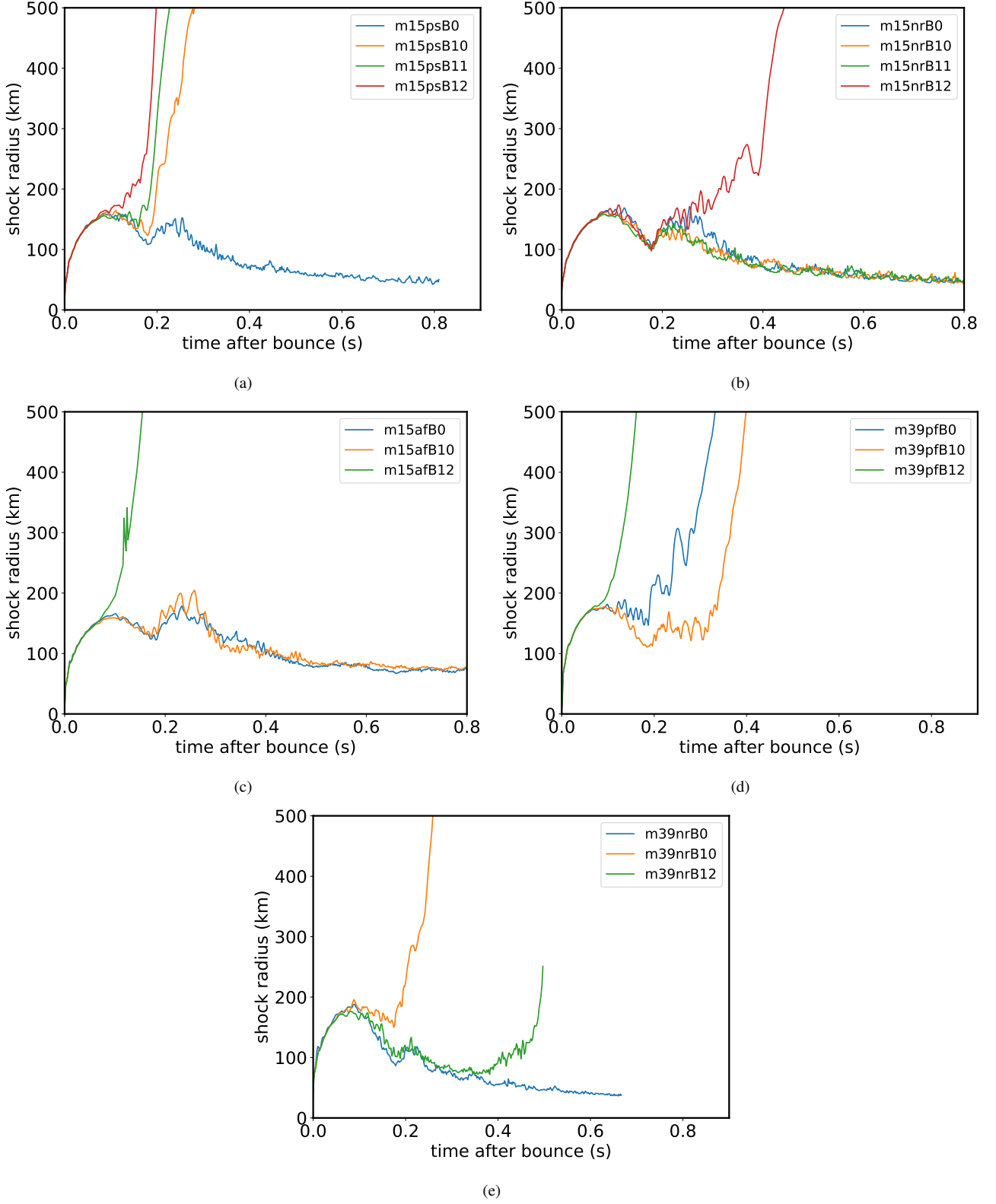


**Figure 2.** Angle-averaged shock radii as a function of post-bounce time for our 15  $M_{\odot}$  and 39  $M_{\odot}$  models. Each panel shows results for one specific rotation profile, but different initial magnetic fields. For 15  $M_{\odot}$  progenitors, models generally tend to explode more readily with increased magnetic field strength, while the impact of rotation is not monotonic. For the 39  $M_{\odot}$  progenitor, the impact of increased magnetic field strength is not monotonic.

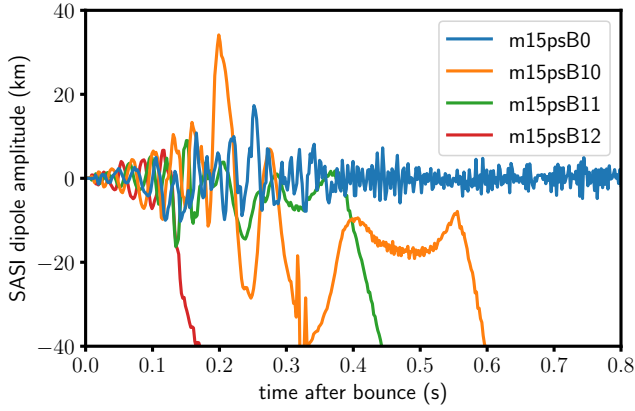


**Figure 3.** SASI diople amplitude for the m15ps models. Despite some fluctuations, models m15psB0 starts out with markedly smaller SASI amplitudes than the other three models prior to the infall of the Si/O shell interface, and therefore fails to start runaway shock expansion shortly afterwards, unlike models m15psB10, m15psB11, and m15psB12.

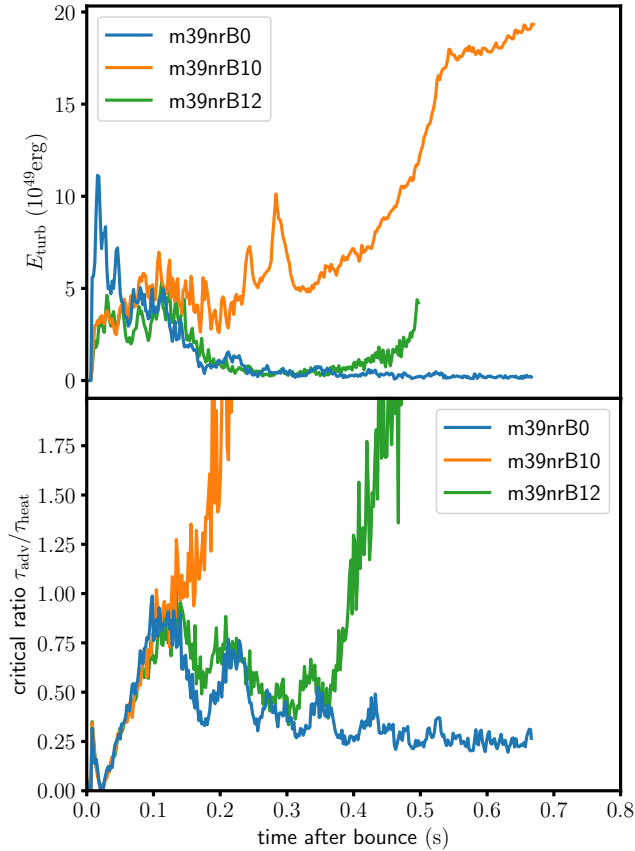


**Figure 4.** The turbulent kinetic energy  $E_{\text{turb}}$  in the gain region and the critical time scale ratio  $\tau_{\text{adv}}/\tau_{\text{heat}}$  for the m39nr models. Model m39nrB12 maintains a lower turbulent kinetic energy in the gain region than model m39nrB10 by the time when  $\tau_{\text{adv}}/\tau_{\text{heat}}$  approaches unity and falls slightly short of an explosive runaway despite similar heating conditions. In model m39nrB0,  $E_{\text{turb}}$  evolves very differently from the other two models with an early peak and a fast decline because of the different seed perturbations from which non-radial instabilities grow (random in m39nrB0 vs. dipolar perturbations from the magnetic field in m39nrB10 and m39nrB12).

The f/g-mode high-frequency emission band is weaker than other models in non-exploding models and sometimes entirely vanishes by 500–600 ms, and there is less power in the p-modes (Morozova et al. 2018) above the dominant high-frequency emission bands. The exception is the m15afB0 case, where the high-frequency emission appears more spread out and longer lasting, although the reason for this is unclear. The non-exploding model m39nrB0 stands apart from the other  $39 M_{\odot}$  in a similar manner (Figure 9d), but, unlike the non-exploding  $15 M_{\odot}$  model, there is no indication of a signal from the SASI.

Some of the rapidly rotating and highly magnetised models show effects in the spectrograms beyond differences in the strength of the f/g-mode or SASI emission band. The highly magnetised models m15psB12 and m39nrB12, still exhibit a clear f/g-mode emission band, but are noteworthy for showing power around this band over a broader range of frequencies compared to non-magnetised and weakly magnetised models. It is possible that the frequency, excitation, coupling of the g- and p-modes above and below the dominant emission band is affected by the presence of strong magnetic fields. For a tentative indication that magnetic fields could be starting to modify the mode structure and the coupling of fluid motions near the bottom of the gain region with oscillation modes, it is instructive to estimate the local Alfvén frequency in the vicinity of the PNS surface. While a detailed analysis of magnetohydrodynamic oscillation modes is complicated, one can estimate the relevant Alfvén frequency  $\omega_A$  for modes with a high radial wave number of order of the inverse of the pressure scale height  $\Lambda$  (cp. Fuller et al. 2015), i.e., for waves mirroring the structure of f/g-modes with predominantly horizontal displacement and a short radial wavelength due to the steep density gradient at the PNS surface,

$$\omega_A \sim \frac{1}{\Lambda} \sqrt{\frac{\langle B_r^2 \rangle}{4\pi\langle \rho \rangle}}. \quad (10)$$

Here angled brackets denote spherical averages. As shown by Figure 10,  $\omega_A$  becomes quite large at densities of  $10^9$ – $10^{11} \text{ g cm}^{-3}$ , which corresponds to the bottom of the gain region, with  $\omega_A/(2\pi)$  reaching a sizeable fraction of the f/g-mode frequency. In the bulk of the convectively stable PNS surface layer at densities of  $10^{11}$ – $10^{13} \text{ g cm}^{-3}$ , which mostly sets the f/g-mode frequency,  $\omega_A$  remains somewhat lower. The scale of  $\omega_A$  suggests a minor influence of magnetic fields on the f/g-mode frequency itself, but a potentially larger role on the interaction of convective motions in the gain region and the f/g-mode and neighbouring modes. However, the power outside the dominant frequency band is still small, so that it is difficult to identify the corresponding dynamic phenomena in the simulation. More simulations are desirable to determine whether the broader distribution of power is a robust feature in strongly magnetised models.

Model m15nrB12 does not exhibit such a broad distribution of power, but shows an indirect impact of magnetic fields on the low-frequency emission band, whose frequency begins to decline shortly after 200 ms simply because the shock starts to expand, whereas the low-frequency emission band in the corresponding models m15nrB0 and m15nrB10 rises monotonically with time due to shock retraction.

Models m15afB0 and m15afB10 illustrate a noteworthy effect of rapid rotation on the mode structure. For non-rotating models, the frequency of the dominant f/g-mode emission band in pseudo-Newtonian simulations is well described by (Müller et al. 2013),

$$f_{\text{peak}} \approx \frac{1}{2\pi} \frac{GM_{\text{by}}}{R_{\text{PNS}}^2} \sqrt{1.1 \frac{m_n}{\langle E_{\bar{\nu}_e} \rangle}}, \quad (11)$$

where  $R_{\text{PNS}}$  is the radius of the PNS,  $E_{\bar{\nu}_e}$  is the electron antineutrino



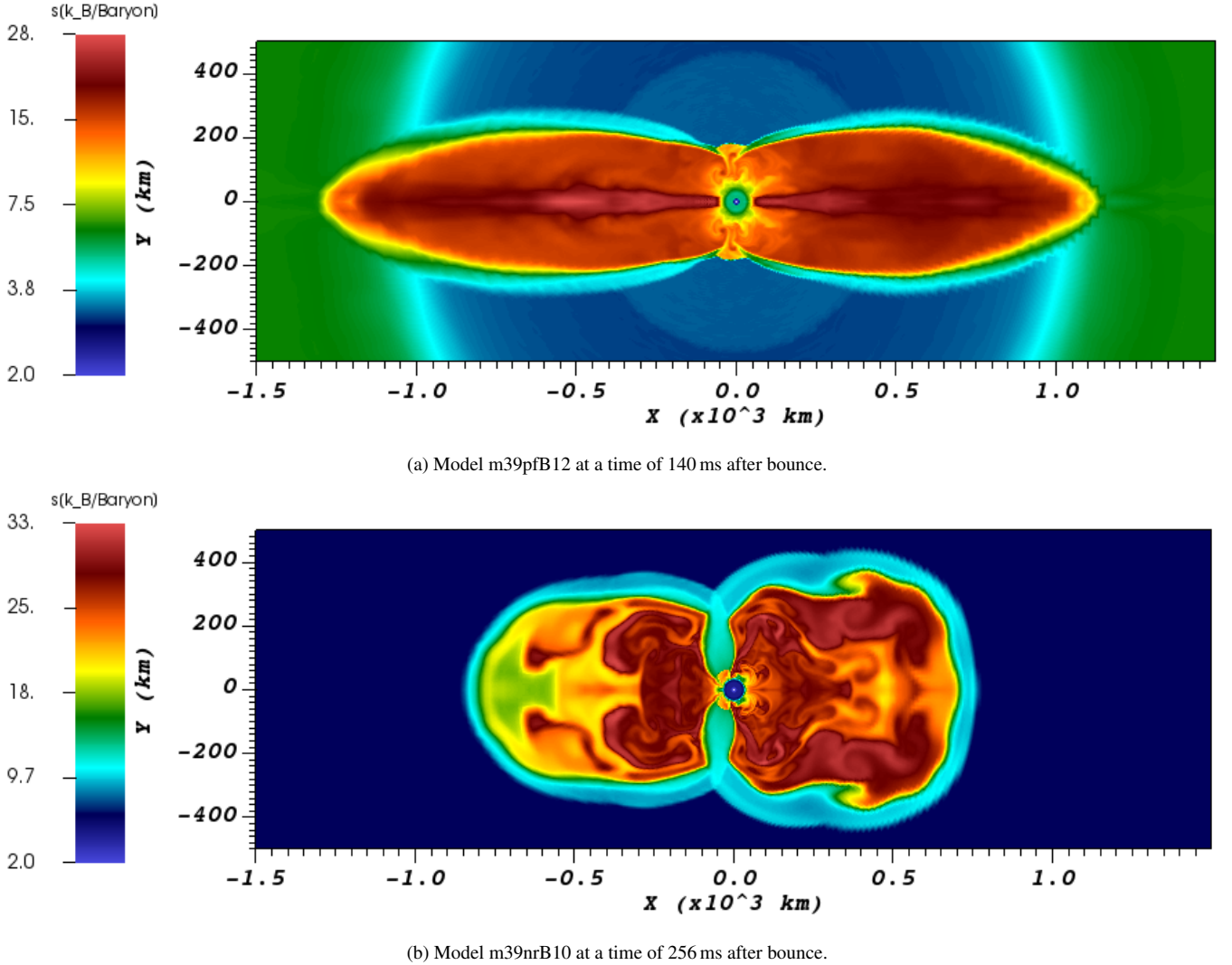


**Figure 5.** 2D entropy snapshots illustrating the different flow structure of model m39pfB12 as an example of a magnetorotational explosion (Panel a), and m39nrB10 as an example of a neutrino-driven explosion (Panel b) at a stage of shock expansion with a similar angle-averaged shock radius.

mean energy,  $m_n$  is the neutron mass and  $M_{\text{by}}$  is the baryonic mass of the PNS. In line with previous 2D and 3D simulations, Equation (11) matches the high-frequency emission band well during the first few hundred milliseconds in almost all models and somewhat overestimates the dominant frequency at late times (black curves in Figures 8 and 9). The m15af models and m39pfB12 are exceptions, however. As illustrated by Figure 11, the predicted frequency from Equation (11) is lowered compared to the non-rotating case for these models mostly because centrifugal support slightly increases the PNS radii and lowers the electron antineutrino mean energy; in case of magnetorotational models, the PNS mass can also be significantly lower than in the non-rotating case because of a rapid explosion and strong mass outflows. The spectrograms do not show the expected decrease in the f/g-mode frequency. In m15afB0 and m15afB10, the dominant emission frequency is up to  $\sim 20\%$  higher than predicted by Equation (11). The higher frequency is consistent with the presence of a positive angular momentum gradient in the region between  $10^{12} \text{ g cm}^{-3}$  and  $10^{13} \text{ g cm}^{-3}$ , which provides additional stabilisation against convection in the PNS surface region. It is noteworthy, though, that the f/g-mode frequency is not shifted upward to the same degree in model m39 despite a positive angular mo-

mentum gradient in this region. Compared to the m39nr models, the dominant frequency still tends to lie slightly higher relative to Equation (11) in the m39 models, but the effect is not as pronounced. It is also interesting that in a 3D model of the  $39 M_{\odot}$  model without magnetic fields, Powell & Müller (2020) found that rotation *decreases* the dominant emission frequency compared to Equation (11). This, however, can be understood based on the detailed dynamics of the models during the explosion phase. In the 3D model of Powell & Müller (2020), a region around the PNS with retrograde rotation emerges due to stochastic variations in the specific angular momentum of accretion downflows. This leads to a negative, destabilising angular momentum gradient at the neutron star surface that lowers the f/g-mode frequency. No such effect occurs in our 2D models. While it may be possible to understand the impact of rotation in more detail for a given simulation by generalising linear perturbation analysis for eigenmodes (Sotani & Takiwaki 2016; Morozova et al. 2018; Torres-Forné et al. 2018) to the rotating case, the disparate results of Powell & Müller (2020) and our study suggest that the impact of rotation on the mode frequencies may be somewhat stochastic and could introduce a generic uncertainty in interpreting

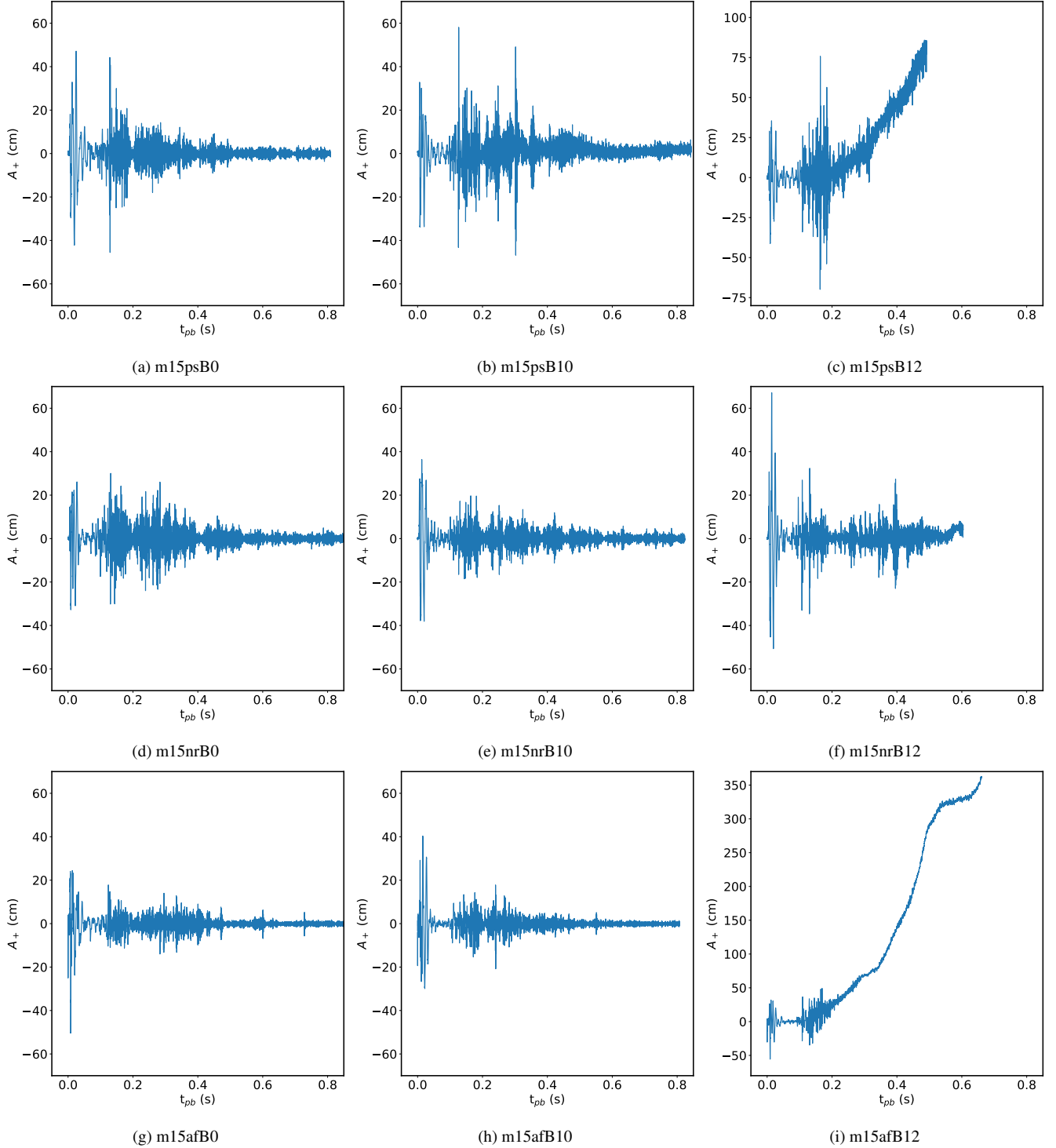


**Figure 6.** Gravitational wave amplitudes  $A_+$  of the plus polarisation mode in the equatorial plane for the  $15 M_\odot$  models. The strong tails present in Panels (c) and (i), with steadily increasing gravitational wave amplitude are a result of a strongly prolate shock expansion in the explosion phase. Note the conspicuous resurgence of high-frequency emission in late times for model m15afB12 in Panel (i). As much as possible, the same scale for  $A_+$  is used for different panels to allow for better comparison, except in Panels (c) and (i) because of the pronounced tail signal.

the f/g-mode frequency of the PNS in rapid rotators if it can be measured.

Finally, the spectrograms of the magnetorotational models m15afB12 and m39pfB12 deviate even more strongly from the familiar picture from extant 2D and 3D simulations. During the pre-

explosion and early explosion phase, they are not remarkable in terms of amplitudes, but the peak emission clearly does *not* follow Equation (11). In model m39pfB12, which has been run for less than 0.3 s post-bounce, one might discern a well-defined emission band with a rapid rise in frequency that certainly does not follow the fa-

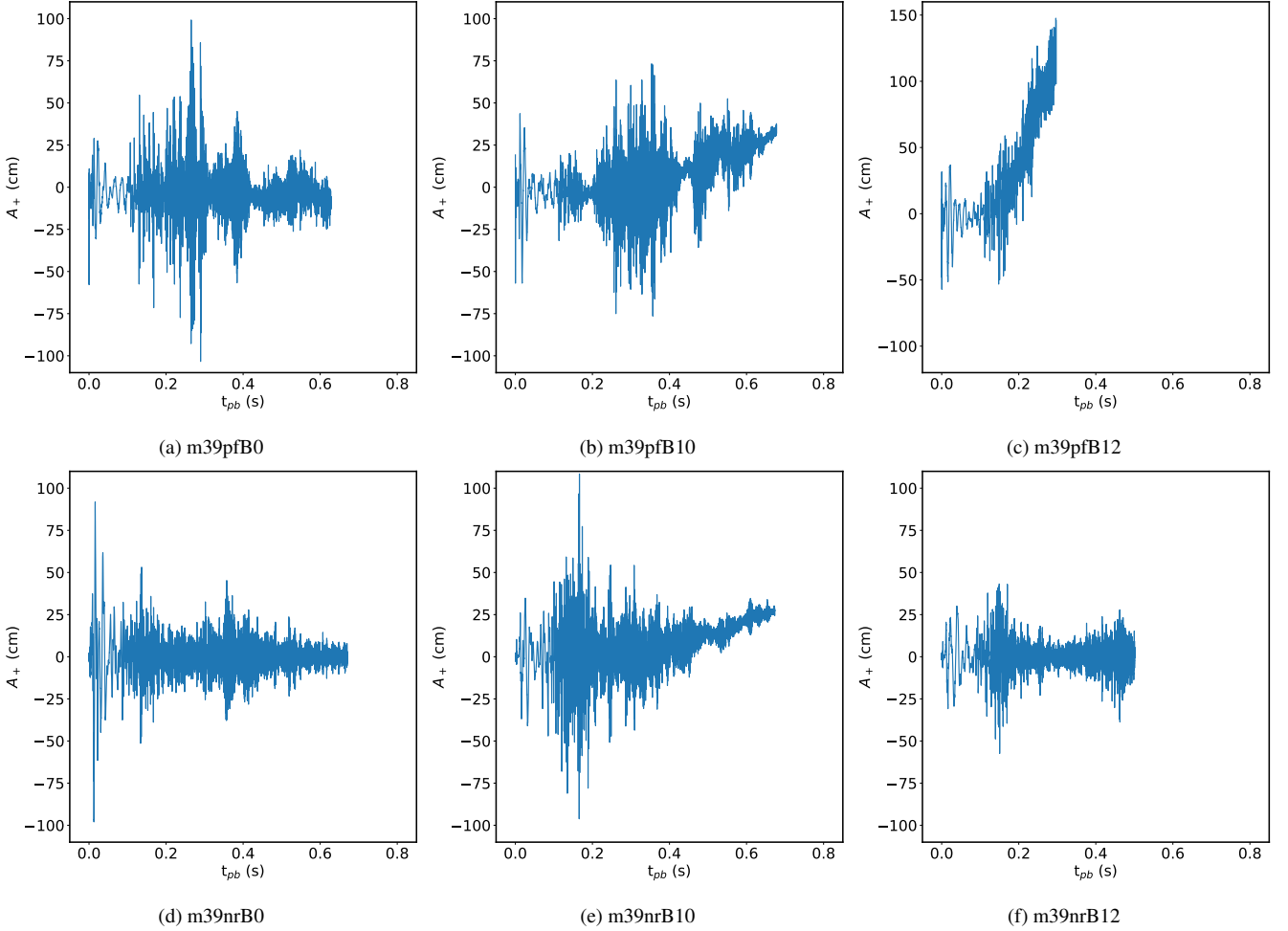


**Figure 7.** Gravitational wave amplitudes  $A_+$  of the plus polarisation mode in the equatorial plane for the  $39 M_\odot$  models. Note again the pronounced tail for the magnetorotational explosion model m39pfB12, similar to model m15afB12 in Figure 6.

miliar f/g-mode frequency relation. In m15afB12, we find a well-defined high-frequency emission band, which is more visibly separated from the predicted trajectory based on Equation (11). There is also considerable power at frequencies below the dominant band, similar to models m15psB12 and m39nrB12. In contrast to these models, rotation and magnetic fields clearly affect the mode structure. A detailed analysis of PNS eigenmodes for the “millisecond magnetars” formed in such models is called for in future, but is beyond the scope of the current, more descriptive study.

#### 4.2.3 Advanced Explosion Phase

The magnetorotational explosion model m15afB12 is also remarkable for its behaviour later on during the explosion phase. All the other exploding models exhibit familiar behaviour, with high-frequency emission tapering off a few hundred milliseconds after shock revival (though some explosion models have not been evolved sufficiently far into the explosion to show this yet), and some of them develop characteristic tails with modest amplitude offsets of a few 10 cm due to aspherical shock expansion (Murphy et al. 2009; Müller et al. 2013). In m15afB12, the tail amplitude is unusually high, reaching 350 cm, and a similarly pronounced tail is developing in model m39pfB12 as well. This tail is the result of the more highly prolate shock geometry in magnetorotational explosions compared

to neutrino-driven explosions (cp. Figure 5). The high-frequency emission subsides as expected due to the termination of accretion downflows that could excite strong PNS oscillations.

Model m39pfB12 still sustains strong high-frequency emission after the onset of explosion. However, the simulation time of this model is relatively short. Model m15afB12, which runs beyond 0.6 s after bounce still shows a clear fingerprint of a dominant f/g-mode in the spectrogram, but high-frequency emission subsides to very low levels once accretion onto the PNS ceases and ceases to excite PNS oscillations.

#### 4.3 Prospects of Detection

To characterise the overall strength and frequency structure of the models as parameters that can potentially be constrained by future GW observations, we provide the total emitted energy  $E_{\text{GW}}$  in GWs, the peak amplitude  $A_{20,\text{max}}^{\text{E2}}$  prior to the tail phase, and the peak frequency  $f_p$  of the time-integrated energy spectrum in Table 1. The energy emitted in GWs can be computed in axisymmetry as (Mueller & Janka 1997),

$$E_{\text{GW}} = \frac{c^3}{G} \frac{1}{32\pi} \int_{-\infty}^{+\infty} \left( \frac{dA_{20}^{\text{E2}}}{dt} \right)^2 dt. \quad (12)$$

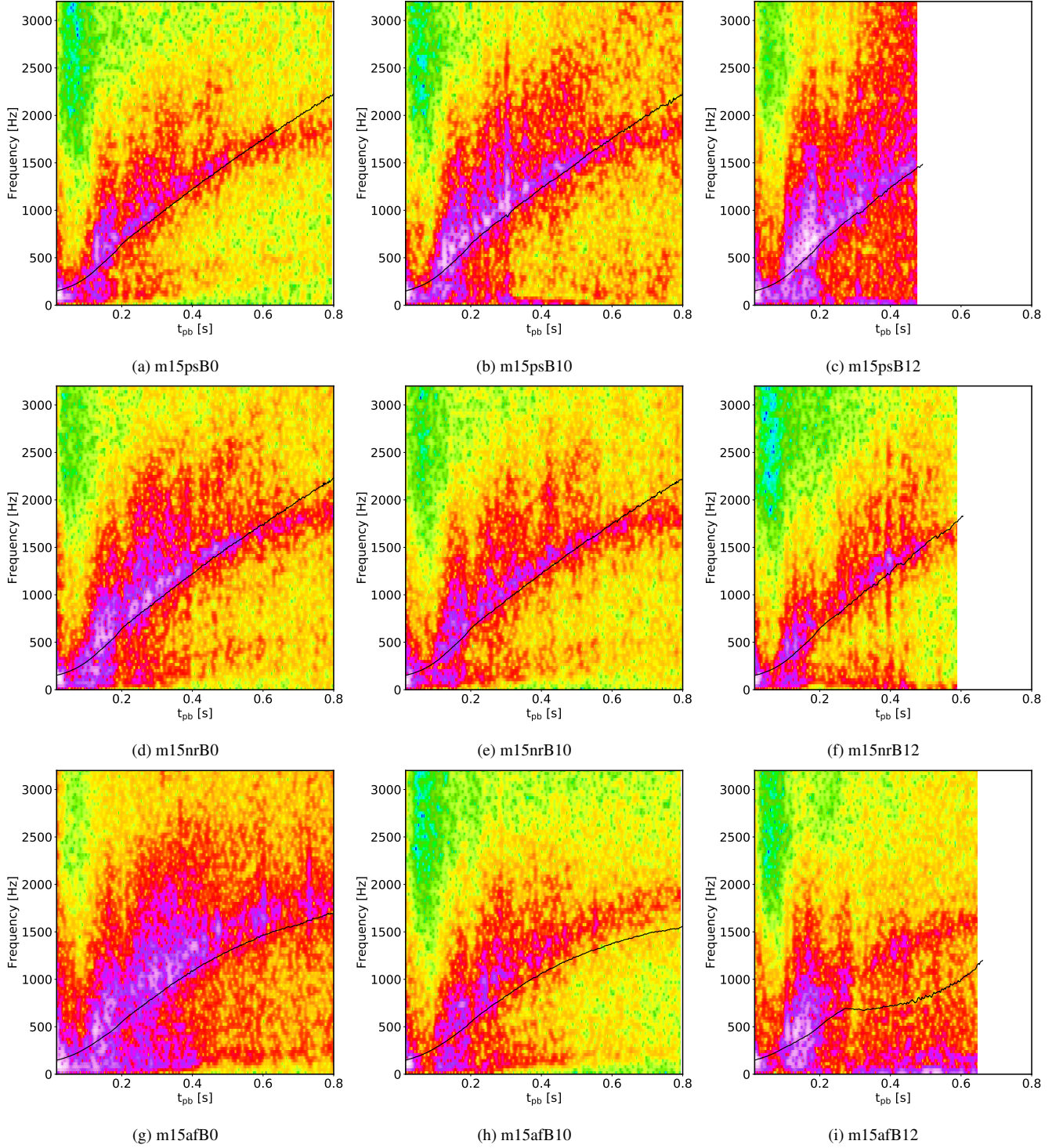


**Figure 8.** GW spectrograms for the  $15 M_{\odot}$  models. Power increases from green to yellow, red, purple, and white. Note the colours of the spectrogram are represented on a logarithmic scale, whose range is not identical for all models. Black curves shows the predicted dominant f/g-mode frequency according to Equation (11). For the non-rotating and moderately rotating models, the analytic relation provides a close fit to the dominant f/g-mode frequency except at late times. For the rapidly rotating models, Equation (11) underestimate the dominant emission frequency in the case of no or moderately strong initial magnetic fields (Panels g and h). For the magnetorotational explosion model m15afB12 (Panel i), one can no longer discern a narrow emission band at high frequencies after a post-bounce time of 0.2 s, and broad-band high-frequency emission appears instead.



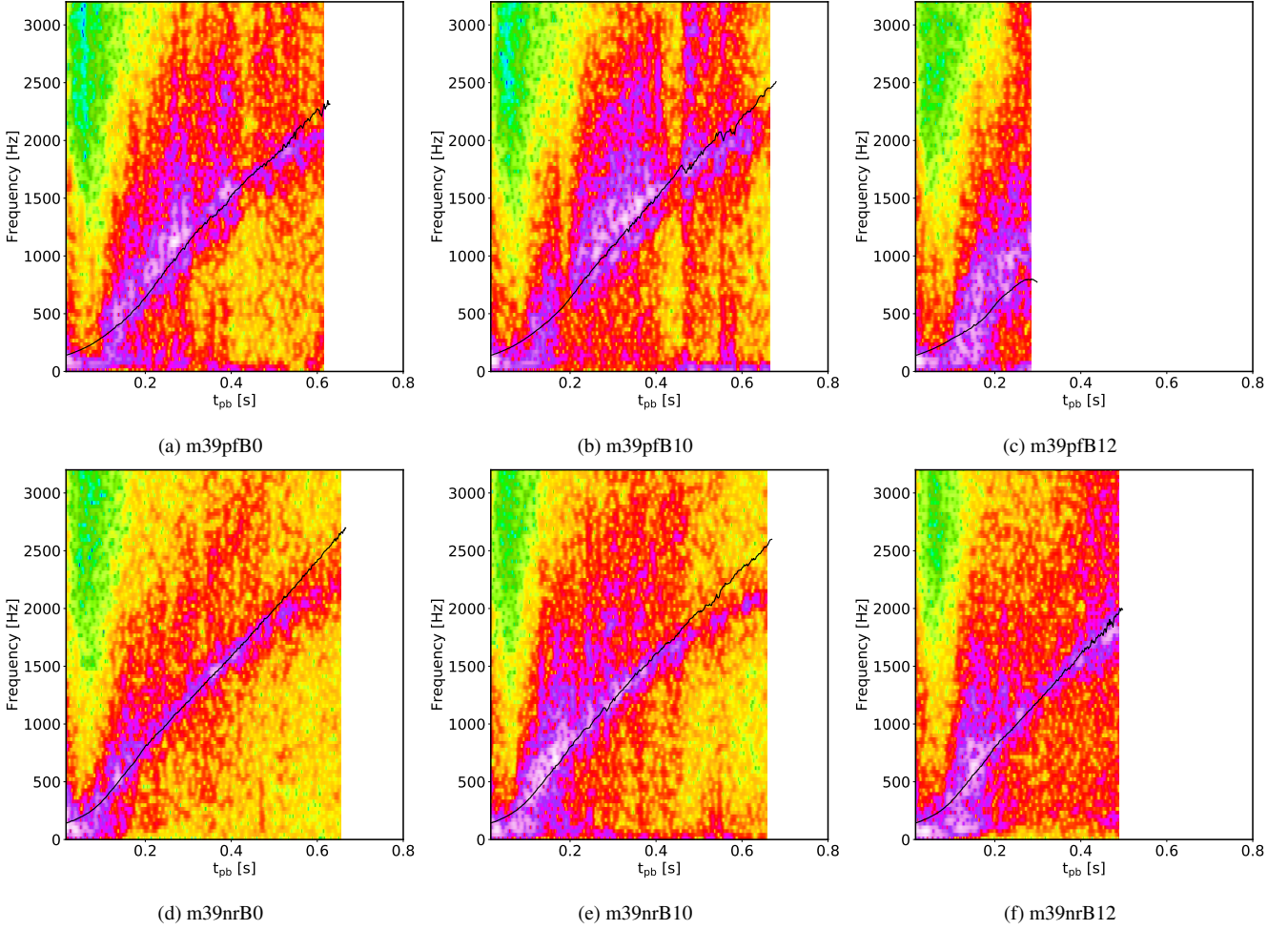


**Figure 9.** GW spectrograms for the  $39 M_{\odot}$  models. Power increases from green to yellow, red, purple, and white. Note the colours of the spectrogram are represented on a logarithmic scale. Black curves shows the predicted dominant f/g-mode frequency according to Equation (11), which fits the high-frequency emission band well except for the magnetorotational explosion model m39pfB12 (Panel c).

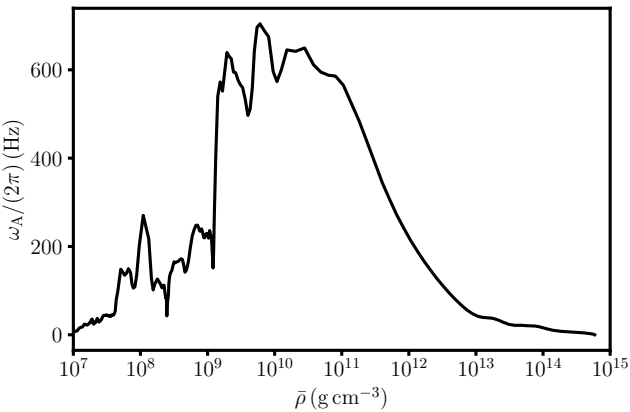


**Figure 10.** Alfvén frequency  $\omega_A$  for modes with a radial wave vector and a wavenumber of the order of the inverse of the pressure scale height (Equation 10) for model m15psB12 at a time of 400 ms after bounce.  $\omega_A$  is shown as a function of the angle-averaged density  $\bar{\rho}$ .

The time-integrated energy spectrum, which is required to determine  $f_p$  is calculated as (Müller et al. 2013),

$$\frac{dE}{df} = \frac{c^3}{16\pi G} (2\pi f)^2 \left| \int_{-\infty}^{\infty} e^{-2\pi i f t} A_{20}^{E2}(t) dt \right|^2, \quad (13)$$

where  $f$  is the frequency.

In most cases,  $E_{\text{GW}}$  is yet to plateau by the end of our simulations. However, we already see trends emerging that are by and large compatible with previous findings in the literature; i.e., exploding models generally have higher GW energies than non-exploding ones (Müller et al. 2013; Radice et al. 2019), and there is a tendency for models which explode earlier to exhibit larger GW energies. These trends are not without exception and subject to significant scatter. For example, the energy emitted in GWs is exceptionally high in model m39nrB0 even though it fails to explode. It is more than twice as high as for the exploding model m39nrB12, which cannot be explained by the slightly longer simulation time. We also see the  $E_{\text{GW}}$  is higher in all  $39 M_{\odot}$  models than in the  $15 M_{\odot}$  cases, again confirming the trend towards stronger GW emission for more massive progenitors found previously in the literature (Müller et al. 2013; Radice et al. 2019).

There are no clear monotonic trends of the emitted GW energy with magnetisation or rotation. The indirect effects of magnetisation and rotation on GW emission through the explosion dynamics fall within stochastic model variations when we consider an integrated measure like  $E_{\text{GW}}$ .

There is also hardly any systematic effect on the peak frequency  $f_p$  of the spectrum, and on the shape of the spectrum, even for the

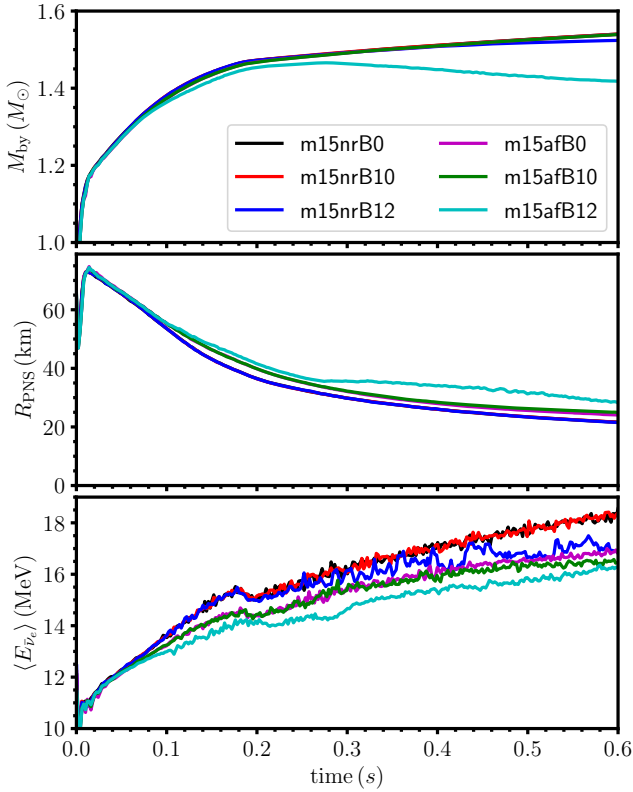


**Figure 11.** PNS parameters entering the analytic relation (11)

for the  $f/g$ -mode frequency for the non-rotating  $15M_{\odot}$  models (m15nr) and the rapidly rotating  $15M_{\odot}$  models (m15af). From top to bottom: Baryonic neutron star mass  $M_{\text{by}}$ , PNS radius  $R_{\text{PNS}}$ , and electron antineutrino mean energy  $\langle E_{\bar{\nu}_e} \rangle$  as a proxy for the PNS surface temperature. The rotating models are characterised by larger PNS radii and lower  $\langle E_{\bar{\nu}_e} \rangle$ . Model m15afB12 also exhibits a significant decrease in PNAS mass at late time due to strong mass outflows.

magnetorotational models m15afB12 and m39pfB12. To illustrate the shape of the time-integrated spectra we plot the characteristic strain  $h_{\text{char}}$  as a quantity that is closely related to the energy spectrum  $dE/df$ , and is also useful for determining the detectability of the waveforms (Flanagan & Hughes 1998):

$$h_{\text{char}}(f) = \sqrt{\frac{2G}{\pi^2 c^3 R^2} \frac{dE}{df}}. \quad (14)$$

Figure 12 shows  $h_{\text{char}}/f^{1/2}$  for all models at a distance of 10 kpc along with the square root of the power spectral density noise  $S(f)$  for Advanced LIGO at design sensitivity (aLIGO; Aasi et al. 2015; Barsotti et al. 2020) and two possible configurations, ET-B and ET-C, for the future Einstein Telescope (Hild et al. 2008, 2010).

For the magnetorotational models m15afB12 and m39pfB12, one would expect a strong reflection of the tail signal in the spectrum; previous studies often found a nearly linear slope on the double-logarithmic scale as in Figure 12, corresponding to a power law in frequency. However, such a power-law spectrum is an artefact of using a rectangular window with a finite duration for Fourier transforming the signal and does not accurately capture the detector response to a slowly varying tail signal. Using a rectangular window introduces a spurious discontinuity in the Fourier-transformed periodic function. No such discontinuity appears in reality; the real signal would vary smoothly before and after the simulated time

window. We experimented with various methods such as continuous padding to verify that the low-frequency power is significantly overestimated using the standard approach. For pragmatic reasons, we follow our previous papers (Powell & Müller 2019, 2020; Powell et al. 2021) and simply apply a high-pass Butterworth filter that removes frequency components below 10 Hz and has a smooth attenuation function above. Model m15afB12 does still show higher power than the other  $15M_{\odot}$  models at low frequency, and it also has a rather low peak frequency of  $f_p = 450$  Hz, but still does not stand apart considerably from the other models.

All the other models exhibit a more familiar shape with a recognisable broad peak around 100 Hz in some models (due to the early quasi-periodic signal and later SASI activity) and a broad distribution of power at high frequencies that usually declines above 1–1.5 kHz.

Based on the characteristic strain, we estimate the detectability of our GW models by computing the optimal signal-to-noise ratio (SNR) from 20–2000 Hz at the typical distance of 10 kpc for a galactic core-collapse supernova. Assuming optimal detector orientation and an observer in the equatorial plane, the SNR can be computed as (Flanagan & Hughes 1998)

$$\langle \text{SNR}^2 \rangle = \frac{15}{8} \int \frac{h_{\text{char}}(f)^2}{h_{\text{RMS}}(f)^2} d \ln f = \frac{15}{8} \int \frac{h_{\text{char}}(f)^2}{f S(f)} d \ln f, \quad (15)$$

where  $h_{\text{RMS}}(f) = \sqrt{f S(f)}$  in terms of the the power spectral density the noise in the detector (Flanagan & Hughes 1998; Moore et al. 2015). Note that an extra factor 15/8 appears for a detector in the equatorial direction compared to Equation (5.2) of Flanagan & Hughes (1998), which involves averaging over source directions (but not over sub-optimal detector orientations). We note that this simple procedure ignores complications like non-stationarity, non-Gaussianity and glitches (for a recent discussion, see Szczepańczyk et al. 2021), and there are also ambiguities due to different possible choices of windowing, padding, and high-pass/low-pass filtering to remove frequencies outside the detector band. Especially the contribution of low-frequency tails to signal detectability must be considered somewhat uncertain. SNRs at a distance of 10 kpc and estimated detection distances based on a threshold SNR of 8 for Advanced LIGO at design sensitivity and configurations ET-B and ET-C of the Einstein Telescope are shown in Table 2. For a non-templatable signal, this condition can predict somewhat too optimistic detection distances, but the criterion still yields indicative results (Flanagan & Hughes 1998; Andresen et al. 2017) in the ballpark of more sophisticated signal analysis methods (Logue et al. 2012; Hayama et al. 2015; Gossan et al. 2016; Powell et al. 2017; Szczepańczyk et al. 2021).

For Advanced LIGO, we obtain detection distances from a few 10 kpc up to about 140 kpc for most of our models. This is within the typical range of detection distances for current CCSN simulations (Gossan et al. 2016; Srivastava et al. 2019; Szczepańczyk et al. 2021), though maybe somewhat on the high side of the distribution. All models would thus be comfortably detectable within the Milky Way with current instruments, and the  $39M_{\odot}$  models would likely remain detectable in the Large Magellanic Cloud at 50 kpc even for non-optimal orientation. With the Einstein Telescope, most waveforms would be detectable in M31 for optimal orientation, and in case of m39nrB0 and m39nrB10 possibly even in the nearest galaxies outside the Local Group (e.g., NGC 300 at 1.9 Mpc). Interestingly, the magnetorotational models m15afB12 and m39pfB12 do not have the highest detection distances. Because of better overlap with the sensitivity range of Advanced LIGO and the Einstein Telescope, the non-rotating models m39nrB0 and m39nrB10 yield

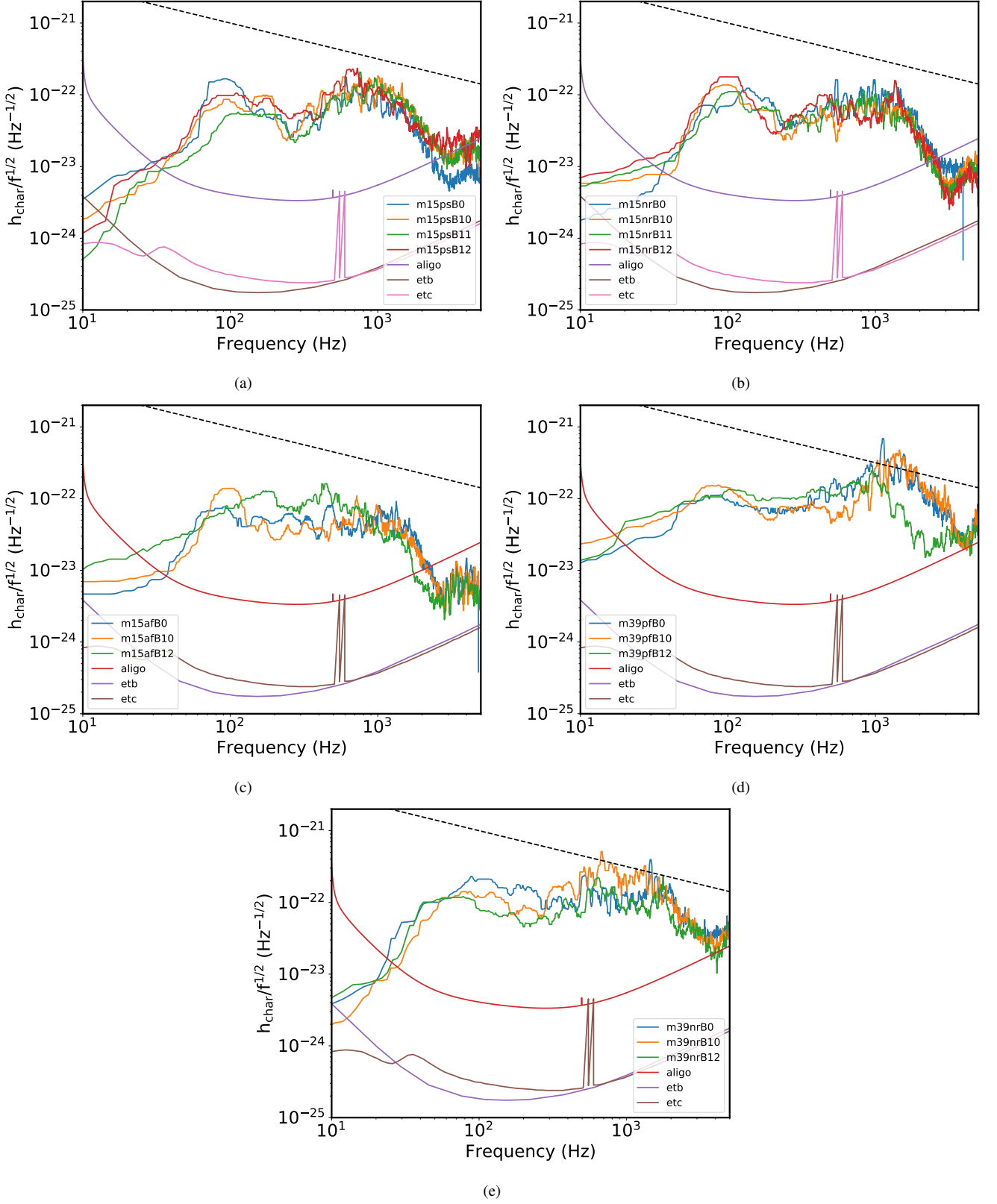


**Figure 12.** The smoothed characteristic GW strain  $h_{\text{char}}$  divided by the square root of the frequency  $f$  for all our models compared to the amplitude spectral density of the detector noise for Advanced LIGO at design sensitivity (aLIGO) and configuration ET-B and ET-C of the Einstein Telescope. The signal curves assume a distance of 10 kpc and an optimal orientation and location of the detector in the equatorial plane of the models. The slope of lines of constant spectral energy density  $dE/df$  is indicated by dashed black lines.

the highest SNRs. It must be borne in mind, however, that strong GW emission is still ongoing by the end of the simulation in case of m39pfB12; and we also have not included the rotational bounce signal. Model m39pfB12 is arguably more representative of hypernova progenitors than m15afB12 with its artificially imposed rotation profile. It therefore stands to reason that this particular magnetorotational models would eventually reach similar detection distances as m39nrB0 and m39nrB10, and be detectable throughout the Local Group. With a fraction of  $\sim 1\%$  of CCSNe exploding as broad-lined Ic “hypernovae” (Smith et al. 2011), putatively powered by some form of magnetorotational explosion, and  $\sim 10$  CCSNe per century (Mattila & Meikle 2001; Srivastava et al. 2019) in the Local Group, this would suggest a chance of about 10% for observing a hypernova in GWs in the next hundred years.

Variations in the maximum detection distance due to the impact of rotation and magnetic fields on the explosion dynamics are modest for the most part. For the  $15 M_{\odot}$  models, detection distances for Advanced LIGO fall between 45 kpc and 85 kpc, i.e., they vary by less than a factor of two. The  $39 M_{\odot}$  models, which generally have SNRs almost twice as high as the  $15 M_{\odot}$  models, show even less of an impact of rotation and magnetic fields on the detection distance, which varies from 82 kpc to 146 kpc.

It is noteworthy that the detection distance for model m39pfB0 is, by and large, comparable to the corresponding 3D model of Powell & Müller (2020). A direct comparison between our model and theirs is not straightforward because they employed the CFC approximation, which leads to a systematic decrease of the f/g-mode frequency in general relativity (Müller et al. 2013). Physically, there are different effects at play in the 2D and 3D models that partly compensate each other with respect to detectability, i.e., lower peak amplitudes in the 3D model, but also a lower f/g-mode frequency due the destabilisation of the PNS surface by a negative angular momentum gradient Powell & Müller (2020), and there are two different polarisation modes in 3D. Overall the comparison between Powell & Müller (2020) and our study illustrates that GW detection distances need not *always* be significantly lower in 3D simulations than in 2D, provided that 3D models explode successfully and develop a pronounced bipolar geometry. However, in many of our models, especially the non-exploding ones, the assumption of 2D axisymmetry may overestimate the wave amplitudes (Andresen et al. 2017): 3D simulations are always required for quantitative accuracy even if 2D models can already reveal trends in GW emission and important features of the waveforms.

The small impact of magnetic fields and the rotation on waveform detectability, even in the extreme case of a magnetorotational explosion, is due to the nature of the prominent signal features that appear in these cases. The pronounced tail signal primarily adds some power at low frequencies. Thus power is added to the spectrum mostly outside the region where Advanced LIGO, Virgo (Acernese et al. 2015), and KAGRA (Akutsu et al. 2020) and planned third-generation detectors like the Einstein Telescope and Cosmic Explorer (Reitze et al. 2019) will be most sensitive.

## 5 CONCLUSIONS

In this work, we conducted 17 different 2D CCSN simulations for  $15 M_{\odot}$  and  $39 M_{\odot}$  progenitor stars with the CoCoNuT-FMT code to study the impact of rotation and magnetic fields on the post-bounce dynamics and GW emission. We considered fast, slow and non-rotating pre-collapse models with initial magnetic field strengths of 0 G,  $10^{10}$  G,  $10^{12}$  G and in two cases  $10^{11}$  G in the progenitor core.

In most cases, we find that strong initial magnetic fields aid the development of explosions independent of the initial rotation rate, in line with previous studies of MHD effects in CCSN simulations of non-rotating progenitors in 2D (Obergaullinger et al. 2014) and 3D (Müller & Varma 2020), and of rapidly rotating progenitors (Winteler et al. 2012; Mösta et al. 2014; Obergaullinger & Aloy 2017, 2020; Kuroda et al. 2020). However, we also found one case where strong magnetic fields delay the development of an explosion by inhibiting the growth of the turbulent kinetic energy in the gain region, similar to the recent study of Matsumoto et al. (2020). The impact of rotation on the post-bounce dynamics tends to be more non-monotonic, e.g., in the  $15 M_{\odot}$  models conditions are more favourable for moderate rotation and less favourable for rapid rotation and no rotation. Again, this is consistent with previous studies of rotational effects on the post-bounce dynamics (Summa et al. 2018). For rapid rotation and strong initial magnetic fields, we find powerful magnetorotational explosions for both progenitors. The rapidly rotating, strongly magnetised  $15 M_{\odot}$  model has reached an explosion energy of  $8.6 \times 10^{51}$  erg by the end of the simulation, and is still growing at an unabated pace.

In all cases, the GW signals from our models exhibit similar patterns as in systematic studies of the post-bounce GW emission from non-rotating, non-magnetised progenitors (Murphy et al. 2009; Müller et al. 2013; Andresen et al. 2017; Morozova et al. 2018; Radice et al. 2019; Powell & Müller 2019; Mezzacappa et al. 2020) with a dominant high-frequency f/g-mode emission band whose power peaks around the onset of explosion, and in some case low-frequency emission from the SASI. Variations in peak amplitude, the total energy emitted in GWs, and the SNR in GW detectors are modest and can be traced to variations in explosion outcome (shock revival vs. failure) or the time and strength of explosion.

Deviations from the usual behaviour are found for rapidly rotating and strongly magnetised models, however. For the rapidly rotating  $15 M_{\odot}$  models, we find that the familiar analytic frequency relation  $f_{\text{peak}} \approx (2\pi)^{-1} GM_{\text{by}}/R_{\text{PNS}}^2 (1.1 m_{\text{n}}/\langle E_{\text{ve}} \rangle)^{1/2}$  for the dominant f/g-mode (Müller et al. 2013) no longer holds because the stabilising influence of a positive angular momentum gradient shifts the mode frequency upward by up to 20%.

For magnetorotational models, the trajectory of the dominant high-frequency emission band bears little resemblance to the standard frequency relation, but a single dominant high-frequency emission mode, likely a modified f/g-mode remains visible in the spectrograms. In the magnetorotational explosion of the  $15 M_{\odot}$  progenitor, high-frequency emission subsides to a low level some time after the onset of the explosion because accretion on the proto-neutron star essentially ceases. Due to their strongly prolate explosion geometry, the matter signal from magnetorotational explosions is characterised by a very pronounced tail signal during the explosion phase. While such a strong tail in the matter signal appears unique to jet-driven explosions, similarly strong tails may arise from anisotropic neutrino emission and therefore cannot be easily used to identify magnetorotational explosions.

The estimated maximum detection distances for our models amount to several 10 kpc to 140 kpc for Advanced LIGO and 0.6–2.6 Mpc for the Einstein Telescope, and fall within the range of predicted detection distances in the literature. The magnetorotational models do not stick out significantly in terms of detectability. The highest detection distances are predicted for neutrino-driven explosion models, although this might yet change for longer simulations because of continued GW emission in the two magnetorotational models. Moreover, the  $15 M_{\odot}$  model may not be representative of hypernova progenitors, as it is based on a “normal” su-



Model	aLIGO		ET-B		ET-C	
	SNR	Range	SNR	Range	SNR	Range
m15psB0	58	73 kpc	1140	1.43 Mpc	760	950 kpc
m15psB10	57	72 kpc	1000	1.25 Mpc	760	950 kpc
m15psB11	47	59 kpc	770	960 kpc	650	810 kpc
m15psB12	70	87 kpc	1210	1.51 Mpc	890	1.12 Mpc
m15afB0	37	46 kpc	690	860 kpc	500	620 kpc
m15afB10	42	53 kpc	850	1.07 Mpc	560	710 kpc
m15afB12	61	77 kpc	1130	1.41 Mpc	820	1.02 Mpc
m15nrB0	52	65 kpc	950	1.18 Mpc	700	880 kpc
m15nrB10	48	61 kpc	970	1.21 Mpc	650	810 kpc
m15nrB11	45	56 kpc	840	1.05 Mpc	600	750 kpc
m15nrB12	62	78 kpc	1250	1.57 Mpc	840	1.04 Mpc
m39pfB0	94	118 kpc	1510	1.88 Mpc	1320	1.65 Mpc
m39pfB10	81	101 kpc	1390	1.74 Mpc	1140	1.42 Mpc
m39pfB12	87	109 kpc	1590	1.99 Mpc	1170	1.46 Mpc
m39nrB0	107	134 kpc	2080	2.6 Mpc	1440	1.8 Mpc
m39nrB10	117	146 kpc	1930	2.42 Mpc	1580	1.98 Mpc
m39nrB12	67	84 kpc	1200	1.50 Mpc	860	1.08 Mpc

**Table 2.** Key waveform parameters of relevance for the detectability of the 17 models. SNR denotes the optimal signal-to-noise ratio of each model calculated according to Equation (15) over the frequency from 20 Hz to 2 kHz at a distance of 10 kpc assuming an optimal location and orientation of the detector for Advanced LIGO at design sensitivity (aLIGO) and configurations ET-B and ET-C of the Einstein Telescope. For all three cases, “range” denotes the estimated maximum detection distance which is obtained by assuming a threshold signal-to-noise ratio of 8.

pernova progenitor with an artificially imposed rotation profile. The magnetorotational explosion of the  $39M_{\odot}$  star would be detectable throughout most of the Local Group. Given the local supernova rate and hypernova fraction, this suggests a chance of 10% per century for observing a hypernova in GWs.

Given the inherent limitations of axisymmetric models, our work is intended as an exploratory and descriptive study that seeks to identify effects of magnetic fields and rotation on the supernova GW signal that should then be followed up further in 3D simulations. Future 3D simulations should address the unusual time-frequency structure of the GW signal and the underlying emission mechanisms in magnetorotational hypernova explosions in more detail. As in the case of rapidly rotating, non-magnetised models (Kuroda et al. 2014; Andresen et al. 2019; Shibagaki et al. 2020) genuinely new features may appear in 3D in the GW signals of hypernovae. In addition to the GW fingerprint of magnetoconvection and  $\alpha$ - $\Omega$  dynamo in the PNS (Raynaud et al. 2022), the magnetic fields generated by the magnetorotational instability (Balbus & Hawley 1991; Akiyama et al. 2003) or dynamo amplification within the gain region or at the PNS surface may leave unexpected traces in the GW signals. Although the odds are stacked against a nearby hypernova explosion, the GW emission may have significant potential to elucidate the nature of an extreme supernova explosion in case of such a lucky event.

## ACKNOWLEDGEMENTS

BM acknowledges support by ARC Future Fellowship FT160100035. JP is supported by the Australian Research Council (ARC) Centre of Excellence for Gravitational Wave Discovery (OzGrav), through project number CE170100004 and by the ARC Discovery Early Career Researcher Award (DECRA) project number DE210101050. This research was undertaken with the assistance of resources and services from the National Computational Infrastructure (NCI), which is supported by the Australian Government. It was supported by resources provided by the Pawsey Supercomputing Centre with funding from the Australian Government and the Government of Western Australia. We acknowledge computer time allocations from NCMAS and ASTAC. Some of this work was performed on the OzSTAR national facility at Swinburne University of Technology. OzSTAR is funded by Swinburne University of Technology and the National Collaborative Research Infrastructure Strategy (NCRIS).

## DATA AVAILABILITY

The data from our simulations will be made available upon reasonable requests made to the authors.

## REFERENCES

- Aasi J., et al., 2015, *Classical and Quantum Gravity*, **32**, 115012
- Abbott B. P., et al., 2016, *Phys. Rev. Lett.*, **116**, 061102
- Abbott B. P., et al., 2017, *ApJ*, **848**, L13
- Abdikamalov E., Gossan S., DeMaio A. M., Ott C. D., 2014, *Phys. Rev. D*, **90**, 044001
- Abdikamalov E., Pagliaroli G., Radice D., 2020, arXiv e-prints, [arXiv:2010.04356](https://arxiv.org/abs/2010.04356)
- Acernese F., et al., 2015, *Classical and Quantum Gravity*, **32**, 024001
- Aguilera-Dena D. R., Langer N., Moriya T. J., Schootemeijer A., 2018, *ApJ*, **858**, 115
- Akiyama S., Wheeler J. C., Meier D. L., Lichtenstadt I. Meier D. L., Lichtenstadt 2003, *ApJ*, **584**, 954
- Akutsu T., et al., 2020, arXiv e-prints, [arXiv:2009.09305](https://arxiv.org/abs/2009.09305)
- Andresen H., Müller B., Müller E., Janka H. T., 2017, *MNRAS*, **468**, 2032
- Andresen H., Müller E., Janka H. T., Summa A., Gill K., Zanolin M., 2019, *MNRAS*, **486**, 2238
- Balbus S. A., Hawley J. F., 1991, *ApJ*, **376**, 214
- Barsotti L., Fritschel P., Evans M., Gras S., 2020, Updated advanced ligo sensitivity design curve 2020, <https://dcc.ligo.org/LIGO-T1800044/public>
- Blackman R. B., Tukey J. W., 1958, *Bell System Technical Journal*, **37**, 185
- Blanchet L., Damour T., Schaefer G., 1990, *MNRAS*, **242**, 289
- Blondin J. M., Mezzacappa A., 2006, *ApJ*, **642**, 401
- Blondin J. M., Mezzacappa A., DeMarino C., 2003, *ApJ*, **584**, 971
- Buras R., Janka H. T., Rampp M., Kifonidis K., 2006, *A&A*, **457**, 281
- Burrows A., Dessart L., Livne E., Ott C. D., Murphy J., 2007, *ApJ*, **664**, 416
- Cerdá-Durán P., DeBrye N., Aloy M. A., Font J. A., Obergaulinger M., 2013, *ApJ*, **779**, L18
- Christensen U. R., Holzwarth V., Reiners A., 2009, *Nature*, **457**, 167
- Dedner A., Kemm F., Kröner D., Munz C.-D., Schnitzer T., Wesenberg M., 2002, *Journal of Computational Physics*, **175**, 645
- Dimmelmeier H., Ott C. D., Marek A., Janka H. T., 2008, *Phys. Rev. D*, **78**, 064056
- Epstein R., 1978, *ApJ*, **223**, 1037
- Ferrario L., Wickramasinghe D., 2006, *MNRAS*, **367**, 1323
- Ferrario L., de Martino D., Gänsicke B. T., 2015, *Space Sci. Rev.*, **191**, 111
- Finn L. S., 1989, in Evans C. R., Finn L. S., Hobill D. W., eds., *Frontiers in Numerical Relativity*, pp 126–145
- Flanagan É. É., Hughes S. A., 1998, *Phys. Rev. D*, **57**, 4535
- Foglizzo T., Galletti P., Scheck L., Janka H.-T., 2007, *ApJ*, **654**, 1006
- Fuller J., Cantiello M., Stello D., Garcia R. A., Bildsten L., 2015, *Science*, **350**, 423
- Gossan S. E., Sutton P., Stuver A., Zanolin M., Gill K., Ott C. D., 2016, *Phys. Rev. D*, **93**, 042002
- Gurski K. F., 2004, *SIAM Journal on Scientific Computing*, **25**, 2165
- Hayama K., Kuroda T., Kotake K., Takiwaki T., 2015, *Phys. Rev. D*, **92**, 122001
- Heger A., Woosley S. E., Spruit H. C., 2005, *ApJ*, **626**, 350
- Hild S., Chelkowski S., Freise A., 2008, arXiv e-prints, [arXiv:0810.0604](https://arxiv.org/abs/0810.0604)
- Hild S., Chelkowski S., Freise A., Franc J., Morgado N., Flaminio R., DeSalvo R., 2010, *Classical and Quantum Gravity*, **27**, 015003
- Kalogera V., et al., 2019, *BAAS*, **51**, 239
- Kippenhahn R., Weigert A., Weiss A., 2012, *Stellar Structure and Evolution*. Springer, Berlin, [doi:10.1007/978-3-642-30304-3](https://doi.org/10.1007/978-3-642-30304-3)
- Kotake K., Kuroda T., 2017, in Alsabti A. W., Murdin P., eds., *Handbook of Supernovae*. Springer International Publishing, p. 1671, [doi:10.1007/978-3-319-21846-5\\_9](https://doi.org/10.1007/978-3-319-21846-5_9)
- Kotake K., Sawai H., Yamada S., Sato K., 2004, *ApJ*, **608**, 391
- Kuroda T., Takiwaki T., Kotake K., 2014, *Phys. Rev. D*, **89**, 044011
- Kuroda T., Kotake K., Takiwaki T., 2016, *ApJ*, **829**, L14
- Kuroda T., Arcones A., Takiwaki T., Kotake K., 2020, *ApJ*, **896**, 102
- Lattimer J. M., Swesty D. F., 1991, *Nuclear Phys. A*, **535**, 331
- Logue J., Ott C. D., Heng I. S., Kalmus P., Scargill J. H. C., 2012, *Phys. Rev. D*, **86**, 044023
- Maeder A., Meynet G., Lagarde N., Charbonnel C., 2013, *A&A*, **553**, A1
- Marek A., Janka H. T., 2009, *ApJ*, **694**, 664
- Marek A., Janka H. T., Müller E., 2009, *A&A*, **496**, 475
- Matsumoto J., Takiwaki T., Kotake K., Asahina Y., Takahashi H. R., 2020, *MNRAS*, **499**, 4174
- Mattila S., Meikle W. P. S., 2001, *MNRAS*, **324**, 325
- Mezzacappa A., et al., 2020, *Phys. Rev. D*, **102**, 023027
- Miyoshi T., Kusano K., 2005, *Journal of Computational Physics*, **208**, 315
- Moore C. J., Cole R. H., Berry C. P. L., 2015, *Classical and Quantum Gravity*, **32**, 015014
- Morozova V., Radice D., Burrows A., Vartanyan D., 2018, *ApJ*, **861**, 10
- Mösta P., et al., 2014, *ApJ*, **785**, L29
- Mösta P., Roberts L. F., Halevi G., Ott C. D., Lippuner J., Haas R., Schnetter E., 2018, *ApJ*, **864**, 171
- Mueller E., Janka H. T., 1997, *A&A*, **317**, 140
- Müller B., Janka H. T., 2015, *MNRAS*, **448**, 2141
- Müller B., Varma V., 2020, *MNRAS*, **498**, L109
- Müller E., Rampp M., Buras R., Janka H.-T., Shoemaker D. H., 2004, *ApJ*, **603**, 221
- Müller B., Dimmelmeier H., Müller E., 2008, *A&A*, **489**, 301
- Müller B., Janka H.-T., Marek A., 2013, *ApJ*, **766**, 43
- Murphy J. W., Ott C. D., Burrows A., 2009, *ApJ*, **707**, 1173
- O'Connor E. P., Couch S. M., 2018, *ApJ*, **865**, 81
- Obergaulinger M., Aloy M. Á., 2017, *MNRAS*, **469**, L43
- Obergaulinger M., Aloy M. Á., 2020, *MNRAS*, **492**, 4613
- Obergaulinger M., Aloy M. Á., 2021, *MNRAS*, **503**, 4942
- Obergaulinger M., Aloy M. A., Müller E., 2006, *A&A*, **450**, 1107
- Obergaulinger M., Janka H.-T., Aloy M. A., 2014, *MNRAS*, **445**, 3169
- Pajkos M. A., Couch S. M., Pan K.-C., O'Connor E. P., 2019, *ApJ*, **878**, 13
- Pan K.-C., Liebendörfer M., Couch S. M., Thielemann F.-K., 2021, *ApJ*, **914**, 140
- Paxton B., et al., 2013, *ApJS*, **208**, 4
- Powell J., Müller B., 2019, *MNRAS*, **487**, 1178
- Powell J., Müller B., 2020, *MNRAS*, **494**, 4665
- Powell J., Szczepančzyk M., Heng I. S., 2017, *Phys. Rev. D*, **96**, 123013
- Powell J., Müller B., Heger A., 2021, *MNRAS*, **503**, 2108
- Radice D., Morozova V., Burrows A., Vartanyan D., Nagakura H., 2019, *ApJ*, **876**, L9
- Rampp M., Janka H. T., 2002, *A&A*, **396**, 361
- Raynaud R., Guilet J., Janka H.-T., Gastine T., 2020, *Science Advances*, **6**, eaay2732
- Raynaud R., Cerdá-Durán P., Guilet J., 2022, *MNRAS*, **509**, 3410
- Reitze D., et al., 2019, in *Bulletin of the American Astronomical Society*, p. 35 ([arXiv:1907.04833](https://arxiv.org/abs/1907.04833))
- Richers S., Ott C. D., Abdikamalov E., O'Connor E., Sullivan C., 2017, *Phys. Rev. D*, **95**, 063019
- Sawai H., Kotake K., Yamada S., 2008, *ApJ*, **672**, 465
- Scheidegger S., Fischer T., Whitehouse S. C., Liebendörfer M., 2008, *A&A*, **490**, 231
- Scheidegger S., Käppeli R., Whitehouse S. C., Fischer T., Liebendörfer M., 2010, *A&A*, **514**, A51
- Shibagaki S., Kuroda T., Kotake K., Takiwaki T., 2020, *MNRAS*, **493**, L138
- Smith N., Li W., Filippenko A. V., Chornock R., 2011, *MNRAS*, **412**, 1522
- Sotani H., Takiwaki T., 2016, *Phys. Rev. D*, **94**, 044043
- Sotani H., Takiwaki T., 2020, *MNRAS*, **498**, 3503
- Spruit H. C., 1999, *A&A*, **349**, 189
- Spruit H. C., 2002, *A&A*, **381**, 923
- Srivastava V., Ballmer S., Brown D. A., Afle C., Burrows A., Radice D., Vartanyan D., 2019, *Phys. Rev. D*, **100**, 043026
- Summa A., Janka H.-T., Melson T., Marek A., 2018, *ApJ*, **852**, 28
- Suwa Y., Takiwaki T., Kotake K., Sato K., 2007, *PASJ*, **59**, 771
- Szczepančzyk M. J., et al., 2021, *Phys. Rev. D*, **104**, 102002
- Takiwaki T., Kotake K., 2011, *ApJ*, **743**, 30
- Takiwaki T., Kotake K., 2018, *MNRAS*, **475**, L91
- Takiwaki T., Kotake K., Suwa Y., 2016, *MNRAS*, **461**, L112
- Thompson C., Duncan R. C., 1993, *ApJ*, **408**, 194
- Thorne K. S., 1980, *Reviews of Modern Physics*, **52**, 299
- Torres-Forné A., Cerdá-Durán P., Passamonti A., Font J. A., 2018, *MNRAS*, **474**, 5272

- Torres-Forné A., Cerdá-Durán P., Obergaulinger M., Müller B., Font J. A.,  
2019, [Phys. Rev. Lett.](#), **123**, 051102
- Winteler C., Käppeli R., Perego A., Arcones A., Vasset N., Nishimura N.,  
Liebendörfer M., Thielemann F.-K., 2012, [ApJ](#), **750**, L22
- Yakunin K. N., et al., 2010, [Classical and Quantum Gravity](#), **27**, 194005
- Yakunin K. N., et al., 2015, [Phys. Rev. D](#), **92**, 084040